Green Chemistry

Accepted Manuscript

ROYAL SOCIETY OF CHEMISTRY

www.rsc.org/greenchem

Journal Name

COMMUNICATION

Ultrathin cobalt phosphide nanosheets as efficient bifunctional catalysts for water electrolysis cell and the origin for cell performance degradation

Received 00th January 20xx,
Accepted 00th January 20xx

DOI: 10.1039/x0xx00000x

www.rsc.org/

Jinfa Chang,[a,b] Liang Liang,[b] Chenyang Li,[b] Minglei Wang,[b] Junjie Ge,[b] Changpeng Liu[b,*] and Wei Xing[a,b,*]

Low-temperature electricity-driven water splitting is an established technology for hydrogen production, yet only few materials are able to catalyze hydrogen and oxygen evolution reactions in the same medium. Herein, ultrathin CoP nanosheets (CoP NS) as durable bifunctional catalysts for electrochemical water splitting are reported. The OER and HER activity for CoP NS/C reaching 10 mA cm^{-2} needs an overpotential of only 0.277 V and 0.111 V in basic solution. What's more, when integrated into a practical anion exchange membrane water electrolysis cell using CoP NS as both anode and cathode catalysts, a current density of 335 mA cm^{-2} at 1.8V is achieved, which is rather competitive to state-of-the-art Pt/IrO_2 catalyst. This work would open a new avenue to explore the use of transition metal phosphide as green and attractive bifunctional catalysts toward mass production of hydrogen fuel for applications.

The intermittent power generation from renewable energy sources (e.g., solar panels, biomass, wind, and wave energy) necessitate the storage of energy in chemical form, where a highly efficient water electrolysis device is an ideal choice. A high overpotential is required for water electrolysis to occur at practical rate, where the energy is predominantly consumed by the H_2O/O_2 half reaction, due to the sluggish kinetics of the four-electron oxidation of two water molecules and the formation of relatively weak oxygen-oxygen bond (oxygen evolution reaction, OER).[1-11] The other half reaction, the hydrogen evolution reaction (HER) occurs at relatively higher rate and has a higher exchange current. However, both OER and HER require the use of low abundance and high cost noble metals, including IrO_2 or RuO_2 for OER and Pt-based catalysts for HER, which inhibit the water electrolysis device from mass production.[12] As a result, the development of new, green and efficient water splitting catalysts based on earth-abundant elements becomes an active area of energy research.[13-17] Promising catalytic material based on earth abundant transition metals have been investigated, among which the development of bifunctional catalysts, i.e., active for both HER and OER, is extremely attractive due to the overcome of reaction resistance for both electrodes, the suitability for working under same electrolyte media, and the simplification of the cell structure by using only one type of catalysts.

Bifunctional catalysts are highly desirable for the development of electrically rechargeable metal/air (or oxygen) batteries,[18-20] such as Li-S batteries,[21] Li-O_2 batteries, [22, 23] Li-Air batteries, [24-28] and Zn-air batteries [29-31]. Recently, efforts on development of bifunctional catalyst used in the so called unitized regenerative fuel cells have been widely studied.[12, 32-47] However, to date, few catalysts are capable of catalyzing both HER and OER in the same media in despite of the significant progress made.[3, 11, 48-55] The Janus Co-based electrocatalyst material has recently been shown as a bifunctional catalyst for water splitting in pH 7 phosphate buffer.[11] The Co oxo hydroxoy phosphate species at reductive potentials and Co-Pi at oxidative potentials were reported to be the active site for HER and OER, respectively.[56] An analogous behavior for amorphous Ni oxo hydroxoy film in pH 9.2 borate buffer has been reported.[55] NiFe LDH has also recently been shown as a bifunctional catalyst for water splitting in alkaline conditions.[3] Tour JM's group found that porous Co phosphide/phosphate thin film (PCPTF) was an effective electrocatalysts in acidic electrolyte for HER and in basic solution for OER.[49] Sun's group use electrodeposited cobalt-phosphorous-derived films as competent bifunctional catalysts for water splitting, where metallic cobalt/cobalt phosphide and cobalt oxide were found active for HER and OER, respectively.[50] Recently, Ni_2P, previously known for its excellent catalytical behavior for hydrodesulfurization (HDS) and hydrodenitrogenation (HDN), has been shown as effective Janus catalyst for water splitting in 1 M KOH, the high activity for HER and OER were attributed to the core–shell (Ni_2P/NiO_x) structure.[57] Similarly, Du's group found that Ni_2P is an effective precursor for water oxidation.[58] Most recently, our group found that surface oxidized CoP nanomaterials, especially, CoP nanorods can act as effective catalyst for OER, and the high activity can be attributed to the formation of a thin layer of

[a] State Key Laboratory of Electroanalytica Chemistry, Changchun Institute of Applied Chemistry, Chinese Academy of Sciences, Changchun 130022, PR China; E-mail: xingwei@ciac.ac.cn; Fax: 86-431-85685653.
[b] Laboratory of Advanced Power Sources, Jilin Province Key Laboratory of Low Carbon Chemical Power Sources, Changchun Institute of Applied Chemistry, Chinese Academy of Sciences, Changchun 130022, PR China;
E-mail: liuchp@ciac.ac.cn.
† Electronic Supplementary Information (ESI) available:. See DOI: 10.1039/x0xx00000x

ultrafine crystalline cobalt oxide on the CoP surface.[59] While these bifunctional catalysts exhibited promising catalytic activity, their performances were all evaluated on an electrode in electrochemical cell, where the current was too low for realistic situation. Therefore, it is of significant importance to design and synthesis bifunctional catalysts that is able to deliver high performance in a real water electrolysis cell, thus confirming the suitability of using Janus catalyst in water eletrolyzer.

Herein, we show that CoP nanosheets (CoP NS), which were prepared using a green and facile approach, can catalyse both OER and HER in alkaline medium with remarkable activity and stability. Specifically, the as-prepared CoP nanosheets achieve a current density of 10 mA cm^{-2} with over-potentials at 0.277 V for OER and 0.111 V for HER, ranking among the most active non-precious catalysts for both reactions. Furthermore, when integrated into a practical water electrolysis cell using anion exchange membrane (AEMWE), a current density of 335 mA cm^{-2} was acquired at 1.8V, which is rather competitive to the cell using IrO_2 anode and Pt black cathode, showing the promising nature of CoP NS in acting as a non-noble bifunctional catalyst. In addition, the origin for cell performance degradation using CoP NS act as bifunctional catalysts was extensive characterized and analysed. The results indicate that CoP NS is promising in replace the platinum-group metals (PGMs) catalysts in the electrochemical water electrolytic devices.

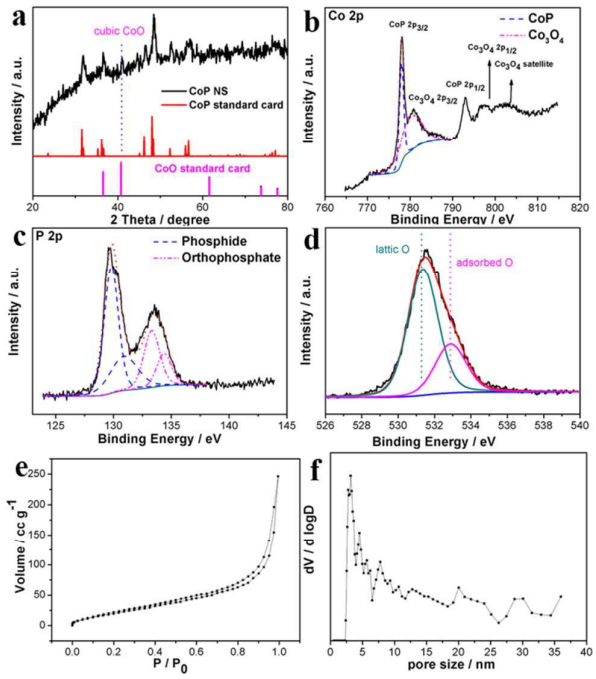

Fig. 1 XRD patterns (a) of CoP NS; high-resolution XPS patterns for (b) Co 2p, (c) P 2p and (d) O 1s of CoP NS; (e) Nitrogen adsorption/desorption isotherm plot of CoP NS and (f) corresponding pore size distribution curves calculated from the desorption branches.

The CoP NS was synthesized by a simple precipitate/low-temperature phosphorization method, using Co_3O_4 as precursor. A passivation process was introduced by passing 1.0 % O_2/N_2 mixture with rate at 20 mL min^{-1} for 3 h (see Experimental Section). Fig. 1a shows the X-ray diffraction (XRD) patterns of as-prepared CoP NS samples, which shows diffraction peaks corresponding to orthorhombic CoP (JCPDS No. 29-0497), the peak at ca. 42° can be assigned to the peak of cubic CoO, in good accordance with the previous reports where Co_3O_4 were converted into CoO under high-temperature treatment.[60] No other prominent features can be detected, indicating the high purity of the CoP NS materials. The crystalline size of CoO was 19.8 ± 1.8 nm and CoP was 13.0 ± 0.5 nm in CoP NS materials calculated with Scherrer formula[61] from the CoO (200) peak at 2 theta ca. 42° and CoP (211) peak at ca. 48.1°. Fig. 1b, c and d are the Co (2p), P (2p) and O (1s) of X-ray photoelectron spectroscopy (XPS) data for CoP NS. The peaks at 778.7 eV and 793.7 eV in Fig. 1b correspond to the Co ($2p_{3/2}$) and Co ($2p_{1/2}$) binding energies, which are close to the BEs of Co in CoP.[62] All other peaks are associated with oxidized cobalt, Co_3O_4, as confirmed in literature [63-65]. The peak at 129.7 eV and 133.6 eV are attributed to phosphide signal and P-O species (orthophosphate), respectively. [62, 63, 66] High-resolution O (1s) region shown in Fig. 1d further confirms the introduction of O to the surface of CoP by oxidizing both elements. XPS results show an atomic ratio of Co:P:O at 47.61: 38.03: 14.36 (Table S1), where Co:P deviates from the stoichiometry of CoP crystalline. The ICP-OES (Table S1) was used to probe the bulky content and a ratio at 1:1 is acquired, corresponding to the CoP phase in the bulk. Combining the XPS and ICP-OES results, it is confirmed that while the bulky content remains unchanged during passivation, Co and P on the surface are oxidized into the $Co^{2/3+}$ and PO_4^{3-}, respectively, according to the surface content ratio measurements. The relative abundance of CoO was 5.1±2.5 (wt %) and CoP was 94.9±2.5 (wt %) in CoP NS material calculated through the ICP and XPS results. Thus, partially surface passivation occurred for CoP NS and this special structure is further used as a candidate bifunctional catalyst both for HER and OER in water splitting.[59] Fig. 1e shows the nitrogen adsorption/desorption isotherm plot of CoP NS, the Brunauer-Emmett-Teller (BET) specific surface area (SSA) of CoP NS was determined to be 95.1 $m^2 g^{-1}$, much bigger than other reported HER/OER catalysts, such as $Ni_{12}P_5$ (42.2 $m^2 g^{-1}$)[67], Ni_2P (48.4 $m^2 g^{-1}$)[67], Ni_5P_4 (54.2 $m^2 g^{-1}$)[67], Ni_2P nanosheet (68.2 $m^2 g^{-1}$)[68], Ni_2P/CNSs (40.7-84.1 $m^2 g^{-1}$)[69], $Co_3O_4/2.7Co_2MnO_4$(85 $m^2 g^{-1}$)[41], NiO (43.6 $m^2 g^{-1}$), Ni_2-Co-O (34.4 $m^2 g^{-1}$), Ni-Co_2-O (24.8 $m^2 g^{-1}$) and bimetallic Ni-Co_2 (32.4 $m^2 g^{-1}$).[70] The Barrett-Joyner-Halenda (BJH) pore size distribution curve (Fig. 1f) of CoP NS confirms the nanoporous/mesoporous nature of CoP NS, which provides numerous catalytic active sites and facilitates electron and mass transport during catalysis process.

The morphology of CoP NS was analysed by Atomic Force Microscope (AFM) on an atomically flat silicon substrate, as shown in Fig. 2a. We analysed AFM topography cross-sections and took the height profiles along two sheets with respect to the substrate to estimate their thickness. The height of the CoP NS is as low as ~3.3 nm, indicating the formation of ultrathin CoP NS. Fig. 2b and Fig. 2c shows typical SEM and TEM images (more images in Fig. S1) for CoP NS, which further confirms the formation of ultrathin CoP NS. The HR-TEM image (Fig. 2d) shows that CoP NS has a lattice fringe with interplane spacing of 0.189 nm, corresponding to the (211) plane of CoP. Inset in framed area of Fig. 2d is a characteristic FFT (Fast Fourier Transformation) image, the dotted framed area

corresponds to the (211) facet of CoP, the spots observed on the FFT are indicative of registry order and crystallinity. The diffraction rings in the SAED pattern (Fig. 2e) recorded from the CoP NS can be identified as the (011), (111), (211) and (301) planes of an orthorhombic CoP structure. Fig. 2f shows the scanning TEM (STEM) image (inset was a magnified STEM) and the corresponding elemental mapping images (Fig. 2g) shows all Co, P and O elements are uniformly distributed across the CoP NS.

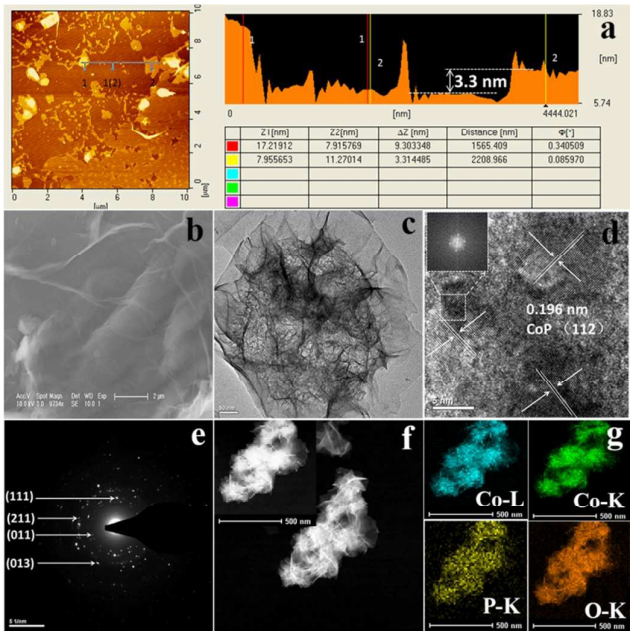

Fig. 2 Semi-contact mode AFM image of CoP NS on an atomically flat silicon substrate, with an individual CoP NS height profile along the gray line shown in the insert. SEM (b), TEM (c), HR-TEM (d), SAED (e), STEM (f), elemental mapping (g) of CoP NS; Inset in framed area of (d) was FFT correspond to the characteristic (211) facet of CoP. The spots observed on the FFT are indicative of registry order and crystallinity. The lattice fringes spacing of the materials were determined using FFT.

The OER activities of the prepared catalysts were firstly evaluated systematically using the typical three-electrode setup by depositing catalysts onto a 0.07 cm^2 GC (glass carbon) electrode in 1 M KOH solution. In order to evaluate the intrinsic catalytic activity of CoP NS, it was physically mixed with carbon (mass ratio, 1:1, CoP NS/C) to enhance the electronic conductivity (Fig. S2) of the electrode. Shown in Fig. S2 is the catalyst loading effect on the electrode performance, where an optimum loading at 0.71 mg cm^{-2} (including CoP NS and carbon) was selected and used as a standard loading for all sequential measurements. A typical four-probe method was used to test the electrical resistance of IrO_2 and CoP nanosheet. The conductivity of CoP nanosheets is at 4.5 S/cm, only about 1/7 that of the commercial IrO_2 (32 S/cm). However, after mixed with carbon (mass ratio, 1:1, CoP NS/C), the conductivity of CoP/C increases to 28 S/cm. Therefore, the lower conductivity of CoP NS can be compensated by mixing with carbon or other conductive materials (Ti felt, for instance, as shown in subsequent discussion), thus achieving its high intrinsic activity. The effect of mass ratio between CoP and C on OER was also investigated as shown in Fig. S3, where a volcano-shaped relationship is revealed and the optimized ratio is 1:1. While mass ratios at >1 provide insufficient electron conductivity, the values at <1 supply insufficient catalytic sites for the reaction, thus leading to inferior performances on both ends. Therefore, the ratio at 1:1 was chosen for all the following performance tests. The catalytic behaviour of CoP NS, CoP NS/C, commercial IrO_2, carbon, and bare GC electrodes are shown in Fig. 3a. As expected, bare GC has no catalytic activity and pure carbon has negligible activity for OER. The onset over-potential for CoP NS, CoP NS/C and IrO_2 are 0.337, 0.253 and 0.296 V (vs. RHE), in sequence. The over-potential at J =10 mA cm^{-2} ($\eta_{@\ J=10\ mA\ cm^{-2}}$) for CoP NS, CoP NS/C, and commercial IrO_2 nanocatalysts (Fig. 3b) are 0.361 V, 0.277 V and 0.320 V, respectively. While the activity of IrO_2 is consistent with the reference value[71, 72], the 0.043 V decrement in over potential for the CoP NS/C in comparison suggests an ultrahigh intrinsic activity for CoP based catalyst, which is higher than most OER catalysts [73] and is the most efficient cobalt based catalysts ever reported (See Table S2). The current density at η = 0.35 V ($J_{@\eta\ =0.35\ V}$) for CoP NS/C, CoP NS and IrO_2 nanoparticles are 43.18, 6.88, and 17.68 mA cm^{-2}, respectively, where the activity of the former is 6.3 and 2.4 times that of the latter two catalysts, further confirms the superior performance of the CoP NS/C. OER charge transfer resistance (R_{CT}) on different catalysts were studied using Electrochemical Impedance Spectroscopy (EIS), where potential dependant EIS spectra for CoP NS and CoP NS/C catalysts are shown in Fig. S4. The R_{CT}, indicated by the arc diameter in Nyquist plots, shows a decreasing trend with increase in over potential due to the constant moving of electron energy to lower values in the electrode and the alteration in valence state of Co. At the same over potential (0.32 V, Fig. 3c), R_{CT} for CoP NS/C (49.5 Ω) is much smaller than that of CoP NS (259 Ω), indicating the huge impact of the electronic conductivity (EC) on the catalyst performance. The EC has long been known to greatly influence the catalytic behaviour of catalysts: the OER performance on Pt, for instance, decrease exponentially with increase in Pt oxide layer thickness (10-15 Å), which was ascribed to the decrease in electron tunnelling and the electron conductivity.[74] The high activity of the CoP NS is rationalized as follows: it is known that transition of the metal cation to higher valence state/higher coordination number catalyses the water electrolysis at the same time. As in the case of Co, the $Co^{III/II}$ and $Co^{IV/III}$ pairs are both possible candidates for OER reaction, with reaction rates to water at 0.19 and >2 s^{-1}, respectively.[56] However, at a given average Co valence, the larger particle/clusters are more stable and resulting in slower kinetics for water oxidation.[75] In the CoP NS catalyst, the surface passivation process led to an ultrathin layer of oxidation (« 1.6 nm), due to the ultrathin nature of the nanosheet (around 3.3 nm, oxidized both sides) and bulk-surface composition deviation observed above. Further, the formation of Co oxide sheet in plane is stunted by the presence of phosphate anions during the passivation process. As a result, more edge and defect sites of Co are acquired, where their coordination numbers are more easily tuned by electrode potential. A similar result can be acquired by using Co-Pi catalyst[49, 50, 56] where enhanced catalytic behaviors are observed, however, the conductivity modification of such film electrodes are difficult to achieve, resulting in inferior activity in comparison to the present CoP NS catalyst. Further, at least three independent measurements

were conducted for the performance tests of CoP NS/C catalysts, where high reproducibility was acquired with polarization curves perfectly overlapping on each other, as shown in Fig. S5a. What's more, from Fig. S5b, it is observed that the error is in allowance range area, which clearly demonstrates the highly reproducible and credible performance of the catalysts.

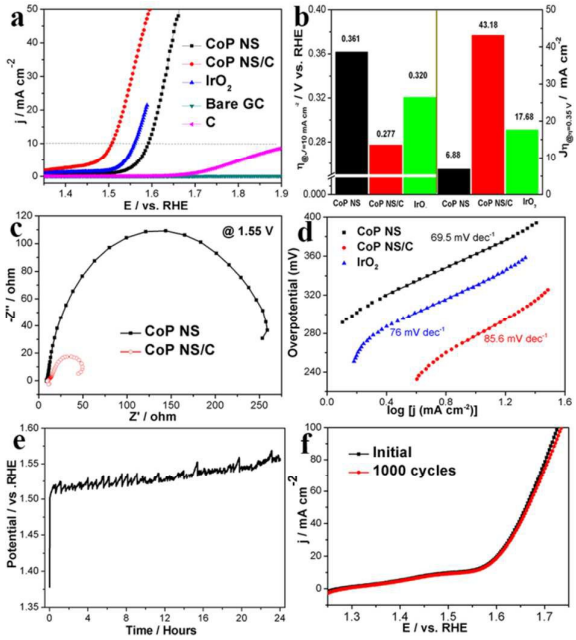

Fig. 3 Polarization curves (a) of the pure CoP NS, the physical mixture of CoP NS and carbon (CoP NS/C), commercial IrO_2 and carbon loaded on GC electrode and bare GC for OER in oxygen saturated 1 M KOH solution, scanning rate was 5 mV s^{-1}; Potentials were corrected with iR drop. (b) Over-potential required for J =10 mA cm^{-2}(η@ J=10 mA cm^{-2}) and current density at η = 0.35 V (J@η =0.35 V) for CoP NS, CoP NS/C and IrO_2 nanoparticles, respectively. Nyquist plots (c) of CoP NS and CoP NS/C at an over-potential of 0.32 V; Tafel slope (d) for CoP NS, CoP NS/C and commercial IrO_2. Time-dependent potential curves (e) for CoP NS/C under a static current density of 10 mA cm^{-2} for 24 hours; polarization curves (f) of initially and after 1000 CV scans between 1.25 and 1.75 V vs RHE with a scanning rate of 100 mV s^{-1}, the iR drop was not corrected.

Further insights into the OER mechanism and possible reaction pathways are accessible through analysing Tafel plots (Fig. 3d). Different Tafel slopes were identified from the CoP NS (69.5 mV dec^{-1}), IrO_2 (76 mV dec^{-1}), and CoP NS/C (85.6 mV dec^{-1}). It is worth noted that although CoP NS/C possesses a much higher catalytic activity than CoP and IrO_2, a higher Tafel slope indicates a second influential factor other than the conductivity modification of carbon. As the oxidation of Co^{II} and/or Co^{III} species are required prior to water oxidation, it is proposed that the oxidation of carbon, although being sluggish and occurs at a slow rate, may acting as a sacrificial material and impedes the water oxidation process by altering the symmetry factor (α). The durability for the CoP NS/C were investigated through a 24 hours (Fig. 3e) galvanostatic measurement at 10 mA cm^{-2} and the continuous cyclic voltammetric (CV) sweeps with potential scan between 1.25 V and 1.75 V at a scan rate of 100 mV s^{-1} for 1000 cycles (Fig. 3f). The slight increase in overpotential shown in both measurements suggested the highly stable nature of the catalysts under high potential. The Faradaic efficiency (FE) of the electrocatalytic oxygen evolution process (Fig. S6 shows an optical photograph about the generation of oxygen bubbles during the CoP NS/C FE test) were analysed by comparing the amount of experimentally quantified oxygen with the theoretically calculated oxygen. As shown in Fig. S7, the agreement between the values suggests an FE close to 100%.

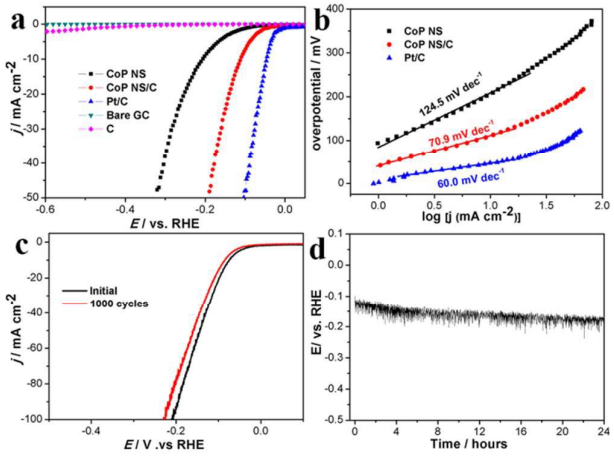

Fig. 4 Polarization curves (a) of the pure CoP NS, the physical mixture of CoP NS and carbon (CoP NS/C), commercial Pt/C and carbon loaded on GC electrode and bare GC for HER in argon saturated 1 M KOH solution, scanning rate was 5 mV s^{-1}; Potentials were corrected with iR drop. (b) Tafel slope for CoP NS, CoP NS/C and commercial Pt/C. Polarization curves (c) of initially and after 1000 CV scans between 0.1 and -0.3 V vs RHE with a scanning rate of 100 mV s^{-1}. Time-dependent potential curves (d) for CoP NS/C under a static current density of 10 mA cm^{-2} for 24 hours; the iR drop was not corrected.

We further assessed the catalytic activity of the CoP NS for HER in the same electrolyte (Figure 4). Same to the OER reaction, a bare GC shows no catalytic activity and pure carbon doesn't show appreciable cathodic current before -0.5 V versus RHE. For all the other catalysts, dramatic increases in HER current densities are observed at potentials < 0 V versus RHE. The over-potential at J =10 mA cm^{-2} ($\eta_{@\ J=10\ mA\ cm^{-2}}$) for CoP NS, CoP NS/C, and commercial Pt/C (Fig. 4b) are 0.207 V, 0.111 V and 0.047 V, respectively. The CoP NS/C reaches current densities of 1, 20, and 50 mA cm^{-2} at η = -0.042, -0.139, and -0.191 V, in sequence. The Tafel slopes (Fig. 4b) at 124.5, 70.9 and 60 mV dec^{-1} for CoP NS, CoP NS/C, and commercial Pt/C were acquired, respectively. The Tafel values for CoP NS/C were much smaller than CoP NS, indicating the high influence of electrode electronic conductivity on the rate of H_2 evolution.[76] It is known to us that electron transport in the catalyst is a separate process from charge transfer reactions, it affects the global activity of a catalyst and is often reflected on high Tafel slopes. For example, Hu's group developed a method based on EIS to identify the slow electron transport process in HER catalysed by molybdenum sulphides, they propose electronic coupling between molybdenum sulphide catalysts and conducting carbon materials

such as graphene, carbon nanotube and graphite can accelerate electron transport in semiconductor MoS_2.[77] As confirmed by Dai and co-workers, they reported a selective solvothermal synthesis of MoS_2 on reduced graphene oxide (RGO) sheets. The resulting MoS_2-RGO hybrid material has a Tafel slope of 41 mV dec^{-1}, much smaller than MoS_2 Nanoparticles (94 mV dec^{-1}) for HER, such decrease was ascribed to the abundant and accessible edge sites of highly dispersed MoS_2 on GO as well as to the enhanced electron transport by coupling graphene sheets to the less-conductive MoS_2 nanoparticles.[78] Similar work was reported such as MoS_2 nanosheets coupling carbon nanotubes[79] and WS_2 coupling RGO[80]. Through the above study, the more favorable HER kinetics on the CoP NS/C is well demonstrated and the performance is also much better than those reported in literature (Table S3). Besides high HER activity, the CoP NS/C catalyst also features excellent stability. Fig. 4c depicts the continuous cyclic voltammetry (CV) results, and after 1000 CV sweeps, the polarization curve showed a negligible change compared with the initial curve. We then investigated the durability of CoP NS/C through chronopotentiometry; the time-dependent voltages under a static current density of 10 mA cm^{-2} are shown in Fig. 4d, which suggest that CoP NS/C maintains the excellent catalytic activity for at least 24 h. Fig. S8 shows the comparison between the H_2 collected, quantified by gas chromatography, and the calculated results from Faraday's Law. The perfectly match of the two plots for the CoP NS/C catalyst indicates a current efficiency at 100%.

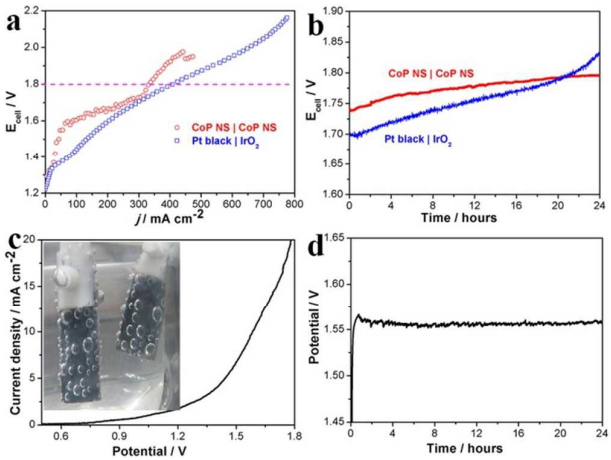

Fig. 5 (a) Polarization curve and (b) cell voltage as a function of test time at current density of 300 mA cm^{-2} for 24 hours of bifunctional CoP NS|CoP NS and a reference Pt black|IrO_2 as cathode and anode catalyst, the catalyst loading of both side was 5 mg cm^{-2}; Operation conditions: T =50 °C and 1 M KOH into the anode-feed with flow rate of 5 mL min^{-1}, both sides are under ambient pressure. Current-potential (c) response of the electrolyzer using CoP NS as catalyst both for OER and HER in 1 M KOH solutions. Two 1*2 cm titanium felt sheet was used as support; Inset was photograph of the electrodes showing the oxygen (left) and hydrogen (right) generation during water electrolysis; Galvanostatic electrolysis (d) in 1 M KOH at a constant current density of 10 mA cm^{-2} over 24 hours.

Upon acquiring high performance for OER and HER, the CoP NS was constructed into a real electrolyzer with anion exchange membrane (AEM) acting as the solid electrolyte. The CoP NS was adopted as both anode and cathode catalyst, where the cell configuration is shown in Fig. S9. For comparison, a reference electrolysis cell using Pt black as cathode and IrO_2 as anode catalyst was also fabricated and tested. The polarization curves are shown in Fig. 5a (see also Fig. S10), a current density at 335 mA cm^{-2} was acquired at 1.8 V using CoP NS|CoP NS MEA, which is rather competitive to the cell using IrO_2 anode and Pt black cathode (413 mA cm^{-2} at 1.8 V in this work), being consistent with previous report where 399 mA cm^{-2} was achieved at 1.8 V in same testing condition[81], but at much lower cost. To the best of our knowledge, this is the first time that a difunctional catalyst is used in a SPE water electrolysis cell and the promising cell performance implies the great potential of CoP NS in replacing the PGMs in the water electrolytic devices for both HER and OER. Furthermore, with possible optimization in cell structure, which is now optimized for Pt/IrO_2 based catalysts, even higher performance is expected for CoP NS. Fig. 5b shows the constant current test of the two cells, where the current density was hold at 300 mA cm^{-2} for 24 hours and the cell voltage was found increased by 56 mV (from 1.739 V to 1.795 V) for using CoP NS|CoP NS MEA, much lower that the cell using Pt black|IrO_2 MEA (138 mV, from 1.695 V to 1.833 V), which further indicate the super stability of the bifunctional CoP NS|CoP NS MEA. The degeneration of IrO_2 and decreased conductivity of anion exchange membrane[81] is proposed to be responsible for the degradation.

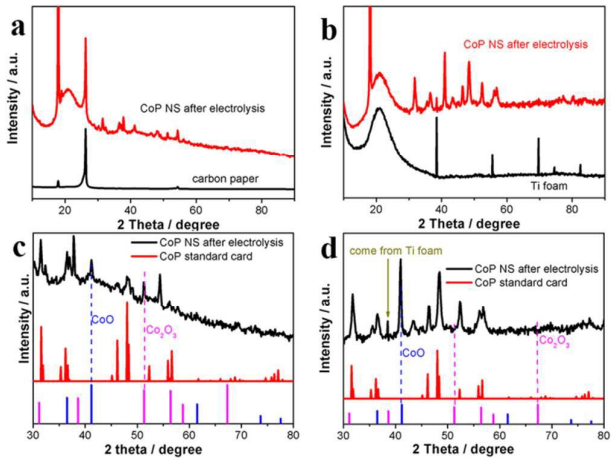

Fig. 6 XRD patterns of CoP NS after electrolysis on anode OER side (a and c) and cathode HER side (b and d).

To further confirm the origin of cell degradation, a two electrode electrolytic cell was constructed using CoP NS as the bifunctional catalysts, where any performance loss can be ascribed to the electrode degradation due to the absence of membrane and the simpler cell construction. It is worth mentioning here that the CoP NS was dispensed on titanium felt sheet (1 cm*2 cm) as the conductive material, where carbon was substituted to further demonstrate the high intrinsic activity of CoP NS. As expected, the current-potential response of the electrolyzer shown in Fig. 6c indicates the highest performance of the bifunctional catalysts ever reported, where a current density of 10 mA cm^{-2} was obtained at

ca. 1.54 V, meaning a combined overpotential of only 0.31 V.[11, 57] Furthermore, the 24 hours galvanostatic electrolysis experiment shown in Fig. 5d indicates the stable nature of the CoP NS catalyst (-10 mV decay) for both HER and OER in two electrode electrolytic cell.

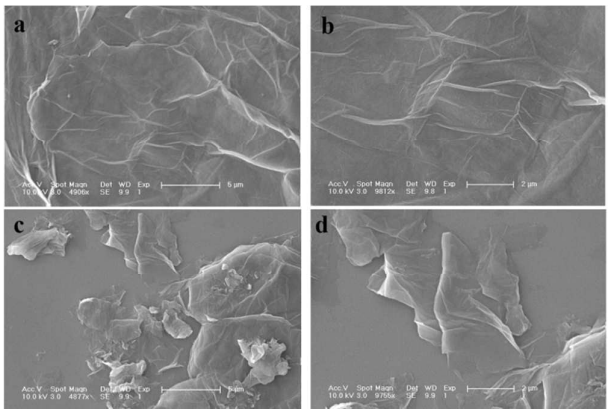

Fig. 7 SEM images of CoP NS after electrolysis on cathode HER side (a and b) and anode OER side (c and d).

In order to further investigate the origin of cell degradation, both the anode and cathode catalysts were examined by XRD, SEM, TEM and XPS characterization after electrolysis at 300 mA cm^{-2} for 24 hours. Fig.6a and Fig.6b are XRD patterns of CoP NS after electrolysis both for anode OER side and cathode HER side; Fig. 6c and Fig. 6d are the enlarged patterns. On the anode OER side, multiple compounds, including CoP, CoO, and Co_2O_3 are noticed after electrolysis, where Co_2O_3 is a newly emerged species. On the cathode HER side, however, only CoP and CoO are observed, and the diffraction patterns are hardly changed from fresh prepared CoP NS. Fig. 7 and Fig. 8 are SEM, TEM, STEM and elemental mapping images after electrolysis. While the catalyst used in cathode side well maintains (Fig.7a,b and Fig. 8a) their original morphology after electrolysis, the anode OER side undergoes serious aggregation and rupture (Fig. 7c,d and Fig. 8c). The aggregation of Co and P can be observed more clearly from the elemental mapping in Fig. 8d.

Furthermore, XPS was also used to probe the change in surface structure of the catalysts after use, as shown in Fig. 9 and Table S4. For the HER side, the content of Co $2p_{3/2}$ (CoP $2p_{3/2}$) increased from 36.73% to 73.49%, and the content of Co_3O_4 $2p_{3/2}$ decreased from 63.27% to 26.51%, respectively. Compare with the freshly prepared CoP NS, it is certified that the metal centers Co (δ^+) had obvious increased, and it had reported that the Co (δ^+) is beneficial for HER[82]. The content and binding energy of all P 2p (phosphide and orthophosphate), and O 1s (lattic O and adsorbed O) has no obvious change after HER electrolysis, indicating a robust and high stability of CoP NS as a HER catalyst. For the OER side, the content of Co $2P_{3/2}$ decreased from 36.73% to 25.10%, while the content of Co_3O_4 $2P_{3/2}$ decreased from 63.27% to 58.03%. Co_3O_4 (Co_2O_3 • CoO) satellite is increased obviously, which is consistent with the XRD results. It is known that for Co, the $Co^{III/II}$ and $Co^{IV/III}$ pairs are both possible candidates for the OER,[56, 59] thus, the increased Co_3O_4 satellite will facilitate the OER performance.[57] The content of phosphide decreased from 66.67% to 22.28% and the content of orthophosphate increased from 33.33% to 77.72%, which is in consistent with previous reports.[83] What's more, the peak position of Co 2p shifted positively by 1.2 eV, while the P 2p peak shifted negatively by 0.7 eV, indicating the occurrence of surface electrons reorganization during the OER electrolysis. However, the content and the binding energy of O 1s exhibit negligible changes (Fig. S11 and Table S4), which may be due to the exposure of the sample to air and soaking in KOH solution[83].

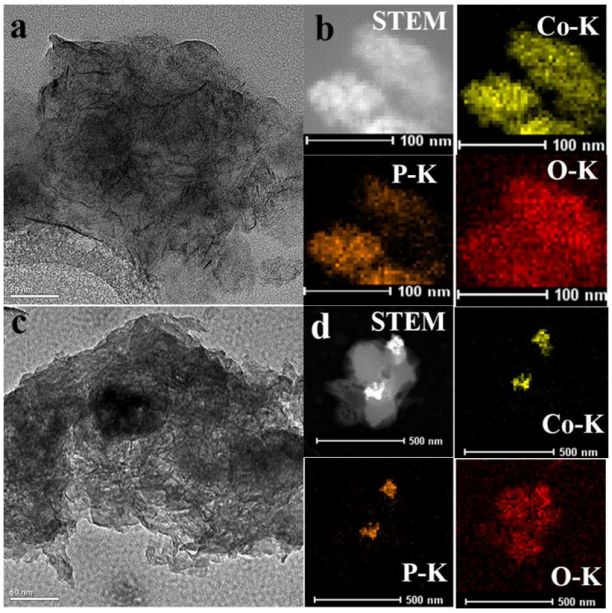

Fig. 8 TEM, STEM and elemental mapping images after electrolysis on cathode HER side (a and b) and anode OER side (c and d).

The structure evolution and the aggregation of the CoP NS at the anode side clearly suggest that the anode degradation contributes to the performance loss of the AEMWE (56 mV). This result is seemingly controversial to two electrode electrolytic cell results shown in above, where the cell potential even decreased by 10 mV after 24 hours electrolysis. The discrepancy between the two measurements can be rationalized as follows: The two electrode electrolytic cell was operated at 10 mA cm^{-2}, with cell voltages located at around 1.54 V. For the AEMWE, however, the current density was held at 300 mA cm^{-2}, and the cell voltages varied in the range of 1.74 to 1.80 V. The much higher over potential results in serious aggregation and rupture of CoP NS used in anode, thus leading to faster cell performance degradation. In addition, we also tested the internal resistance of electrolysis cell before and after electrolysis, and the value was 0.1618 Ω and 0.3745 Ω, respectively. Hence, the deterioration in interfacial contact and membrane degradation are also important factors for the

performance loss. Combining the above analysis, it is convincing that the performance loss of AEMWE is resulted from CoP NS aggregation on anode side, loss in interfacial contact, and membrane degradation.

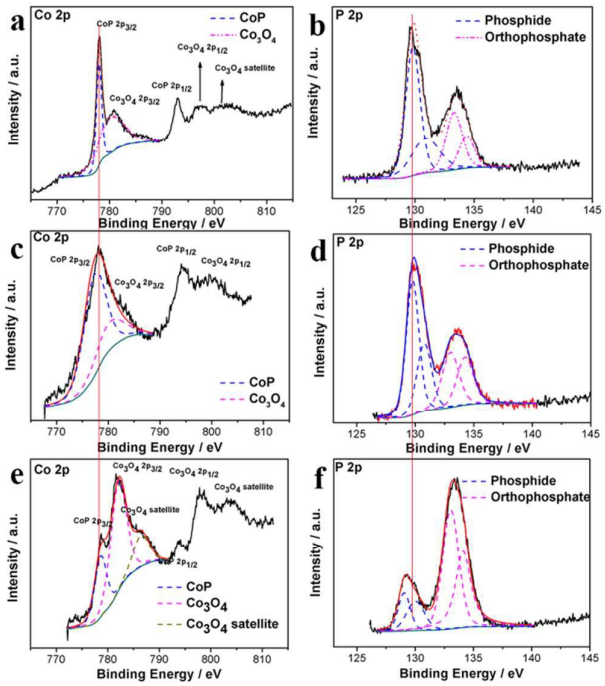

Fig. 9 Comparison the high-resolution XPS patterns for Co 2p (a, c and e) and P 2p (b, d and f) of the fresh prepared CoP NS (a and b) with the CoP NS that after electrolysis on cathode HER side (c and d) and anode OER side (e and f).

In summary, ultrathin CoP NS was prepared by a green and facile approach and found to be an effective and robust catalyst material for overall water splitting. Physical characterization revealed that the CoP NS with a surface passivation was responsible for the superior performance for OER. The unique nanoporous structure of CoP NS can provide numerous catalytically active sites and facilitate electron and mass transport during catalytic tests. The OER and HER activity for CoP NS/C is superior to most state-of-the-art catalysts, where reaching 10 mA cm^{-2} only need an over-potential of 0.277 V and 0.111 V for OER and HER, respectively. Furthermore, the mixed over-potential for a two-electrode electrolytic cell using CoP NS to catalyze both HER and OER was only 0.31 V at a current density of 10 mA cm^{-2}, which is the best result ever reported for a bifunctional catalyst. More importantly, when integrated into a practical AEMWE use CoP NS both for anode and cathode catalyst, the current density was 335 mA cm^{-2} at 1.8 V, which is rather competitive to the state-of-the-art Pt/IrO_2 catalyst at much lower cost. These findings highlight the potential of CoP NS as earth-abundant, cost-effective, eco-friendly and bifunctional catalysts of future (photo) electrochemical water splitting devices and can simplify splitting devices thus promote mass production in energy devices.

Acknowledgements

The authors greatly appreciate the referee for the very constructive comments and insightful suggestions on this manuscript. The work is supported by the National High Technology Research and Development Program of China (863 Program, 2012AA053401), the National Natural Science Foundation of China (21373199, 21433003), the Strategic priority research program of CAS (XDA09030104), Jilin Province Science and Technology Development Program (20130206068GX，20140203012SF) and the Recruitment Program of Foreign Experts (WQ20122200077).

Notes and references

1. M. W. Kanan and D. G. Nocera, *Science*, 2008, **321**, 1072-1075.
2. J. S. untivich, K. J. May, H. A. G. steiger, J. B. Goodenough and Y. n. S. hao-Horn, *Science*, 2011, **334**, 1383-1385.
3. J. Luo, J.-H. Im, M. T. Mayer, M. Schreier, M. K. Nazeeruddin, N.-G. Park, S. D. Tilley, H. J. Fan and M. Grätzel, *Science*, 2014, **345**, 1593-1596.
4. H. Tong, S. Ouyang, Y. Bi, N. Umezawa, M. Oshikiri and J. Ye, *Adv. Mater.*, 2012, **24**, 229-251.
5. J. Deng, P. Ren, D. Deng, L. Yu, F. Yang and X. Bao, *Energy Environ. Sci.*, 2014, **7**, 1919-1923.
6. S. Park, Y. Shao, J. Liu and Y. Wang, *Energy Environ. Sci.*, 2012, **5**, 9331.
7. M. Wang, L. Chen and L. Sun, *Energy Environ. Sci.*, 2012, **5**, 6763-6778.
8. T.-C. Wen and C.-C. Hu, *J. Electrochem. Soc.*, 1992, **139**, 2158-2163.
9. T. E. Mallouk, *Nat Chem*, 2013, **5**, 362-363.
10. L. Grande, E. Paillard, J. Hassoun, J. B. Park, Y. J. Lee, Y. K. Sun, S. Passerini and B. Scrosati, *Adv. Mater.*, 2015, **27**, 784-800.
11. S. Cobo, J. Heidkamp, P. A. Jacques, J. Fize, V. Fourmond, L. Guetaz, B. Jousselme, V. Ivanova, H. Dau, S. Palacin, M. Fontecave and V. Artero, *Nat Mater*, 2012, **11**, 802-807.
12. X. Han, F. Cheng, T. Zhang, J. Yang, Y. Hu and J. Chen, *Adv. Mater.*, 2014, **26**, 2047-2051.
13. B. K. Barman and K. K. Nanda, *Green Chem.*, 2015, **DOI: 10.1039/c5gc01405k**.
14. Y.-P. Yuan, L.-S. Yin, S.-W. Cao, L.-N. Gu, G.-S. Xu, P. Du, H. Chai, Y.-S. Liao and C. Xue, *Green Chem.*, 2014, **16**, 4663-4668.
15. C. Meng, Z. Liu, T. Zhang and J. Zhai, *Green Chem.*, 2015, **17**, 2764-2768.
16. P. V. Cherepanov, I. Melnyk, E. V. Skorb, P. Fratzl, E. Zolotoyabko, N. Dubrovinskaia, L. Dubrovinsky, Y. S. Avadhut, J. Senker, L. Leppert, S. Kümmel and D. V. Andreeva, *Green Chem.*, 2015, **17**, 2745-2749.
17. J. Chen, S. Shen, P. Wu and L. Guo, *Green Chem.*, 2015, **17**, 509-517.
18. L. Jörissen, *J. Power Sources*, 2006, **155**, 23-32.
19. W. G. Hardin, D. A. Slanac, X. Wang, S. Dai, K. P. Johnston and K. J. Stevenson, *J Phys Chem Lett*, 2013, **4**, 1254-1259.
20. Z. Chen, A. Yu, D. Higgins, H. Li, H. Wang and Z. Chen, *Nano letters*, 2012, **12**, 1946-1952.
21. C. Tang, Q. Zhang, M. Q. Zhao, J. Q. Huang, X. B. Cheng, G. L. Tian, H. J. Peng and F. Wei, *Adv Mater*, 2014, **26**, 6100-6105.
22. W. H. Ryu, T. H. Yoon, S. H. Song, S. Jeon, Y. J. Park and I. D. Kim, *Nano letters*, 2013, **13**, 4190-4197.

23. F. Li, R. Ohnishi, Y. Yamada, J. Kubota, K. Domen, A. Yamada and H. Zhou, *Chem Commun (Camb)*, 2013, **49**, 1175-1177.
24. L. Wang, X. Zhao, Y. Lu, M. Xu, D. Zhang, R. S. Ruoff, K. J. Stevenson and J. B. Goodenough, *J. Electrochem. Soc.*, 2011, **158**, A1379.
25. C. Sun, F. Li, C. Ma, Y. Wang, Y. Ren, W. Yang, Z. Ma, J. Li, Y. Chen, Y. Kim and L. Chen, *J. Mater. Chem. A*, 2014, **2**, 7188.
26. W. Yang, J. Salim, S. Li, C. Sun, L. Chen, J. B. Goodenough and Y. Kim, *J. Mater. Chem.*, 2012, **22**, 18902.
27. W. Yang, J. Salim, C. Ma, Z. Ma, C. Sun, J. Li, L. Chen and Y. Kim, *Electrochem commun.*, 2013, **28**, 13-16.
28. L. Wang, M. Ara, K. Wadumesthrige, S. Salley and K. Y. S. Ng, *J. Power Sources*, 2013, **234**, 8-15.
29. G. Du, X. Liu, Y. Zong, T. S. Hor, A. Yu and Z. Liu, *Nanoscale*, 2013, **5**, 4657-4661.
30. X. Liu, M. Park, M. G. Kim, S. Gupta, G. Wu and J. Cho, *Angew. Chem. Int. Ed.*, 2015, **54**, 9654-9658.
31. D. U. Lee, J.-Y. Choi, K. Feng, H. W. Park and Z. Chen, *Adv. Energy Mater.*, 2014, **4**, 1301389.
32. F. Liu, J. Y. Lee and W. J. Zhou, *Small*, 2006, **2**, 121–128.
33. J. Rossmeisl, P. Ferrin, G. A. Tritsaris, A. U. Nilekar, S. Koh, S. E. Bae, S. R. Brankovic, P. Strasser and M. Mavrikakis, *Enery Environ. Sci.*, 2012, **5**, 8335.
34. Q. Liu, J. Jin and J. Zhang, *ACS Appl. Mater. Interfaces*, 2013, **5**, 5002-5008.
35. K. Sakaushi, T. P. Fellinger and M. Antonietti, *ChemSusChem*, 2015, **8**, 1156-1160.
36. F.-D. Kong, S. Zhang, G.-P. Yin, Z.-B. Wang, C.-Y. Du, G.-Y. Chen and N. Zhang, *Int. J. Hydrogen Energy*, 2012, **37**, 59-67.
37. Y. Meng, W. Song, H. Huang, Z. Ren, S. Y. Chen and S. L. Suib, *J. Am. Chem. Soc.*, 2014, **136**, 11452-11464.
38. Y. Gorlin and T. F. Jaramillo, *J. Am. Chem. Soc.*, 2010, **132**, 13612–13614.
39. C. Jin, F. Lu, X. Cao, Z. Yang and R. Yang, *J. Mater. Chem. A*, 2013, **1**, 12170.
40. Y. J. Sa, K. Kwon, J. Y. Cheon, F. Kleitz and S. H. Joo, *J. Mater. Chem. A*, 2013, **1**, 9992.
41. D. Wang, X. Chen, D. G. Evans and W. Yang, *Nanoscale*, 2013, **5**, 5312-5315.
42. G. L. Tian, M. Q. Zhao, D. Yu, X. Y. Kong, J. Q. Huang, Q. Zhang and F. Wei, *Small*, 2014, **10**, 2251-2259.
43. Y. Gorlin, B. Lassalle-Kaiser, J. D. Benck, S. Gul, S. M. Webb, V. K. Yachandra, J. Yano and T. F. Jaramillo, *J. Am. Chem. Soc.*, 2013, **135**, 8525-8534.
44. E. Negro, S. Polizzi, K. Vezzù, L. Toniolo, G. Cavinato and V. Di Noto, *Int. J. Hydrogen Energy*, 2014, **39**, 2828-2841.
45. V. Di Noto, E. Negro, S. Polizzi, F. Agresti and G. A. Giffin, *ChemSusChem*, 2012, **5**, 2451-2459.
46. E. Negro, K. Vezzù, F. Bertasi, P. Schiavuta, L. Toniolo, S. Polizzi and V. Di Noto, *ChemElectroChem*, 2014, **1**, 1359-1369.
47. T. Maiyalagan, K. A. Jarvis, S. Therese, P. J. Ferreira and A. Manthiram, *Nat. Commun.*, 2014, **5**, 3949.
48. X. Liu, H. Zheng, Z. Sun, A. Han and P. Du, *ACS. catal.*, 2015, **5**, 1530-1538.
49. Y. Yang, H. Fei, G. Ruan and J. M. Tour, *Adv. Mater.*, 2015, **27**, 3175-3180.
50. N. Jiang, B. You, M. Sheng and Y. Sun, *Angew. Chem. Int. Ed.*, 2015, **54**, 6251-6254.
51. M. Ledendecker, S. Krick Calderon, C. Papp, H. P. Steinruck, M. Antonietti and M. Shalom, *Angew. Chem. Int. Ed.*, 2015, **127**, 12538-12542.
52. C. Tang, N. Cheng, Z. Pu, W. Xing and X. Sun, *Angew. Chem. Int. Ed.*, 2015, **127**, 9483-9487.
53. H. Jin, J. Wang, D. Su, Z. Wei, Z. Pang and Y. Wang, *J. Am. Chem. Soc.*, 2015, **137**, 2688-2694.
54. D. Liu, Q. Lu, Y. Luo, X. Sun and A. M. Asiri, *Nanoscale*, 2015, **7**, 15122-15126.
55. C. He, X. Wu and Z. He, *J. Phys. Chem. C*, 2014, **118**, 4578-4584.
56. H. S. Ahn and A. J. Bard, *J. Am. Chem. Soc.*, 2015, **137**, 612-615.
57. L.-A. Stern, L. Feng, F. Song and X. Hu, *Energy Environ. Sci.*, 2015, **8**, 2347-2351.
58. A. Han, H. Chen, Z. Sun, J. Xu and P. Du, *Chem. Comm*, 2015, **51**, 11626-11629.
59. J. Chang, Y. Xiao, M. Xiao, J. Ge, C. Liu and W. Xing, *ACS. catal.*, 2015, **5**, 6874-6878.
60. Y. Wang, T. Zhou, K. Jiang, P. Da, Z. Peng, J. Tang, B. Kong, W.-B. Cai, Z. Yang and G. Zheng, *Adv. Energy Mater.*, 2014, **4**, 1400696.
61. A. Patterson, *Physical review*, 1939, **56**, 978.
62. A. P. Grosvenor, S. D. Wik, R. G. Cavell and A. Mar, *Inorg. Chem.*, 2005, **44**, 8988-8998.
63. F. H. Saadi, A. I. Carim, E. Verlage, J. C. Hemminger, N. S. Lewis and M. P. Soriaga, *J. Phys. Chem. C*, 2014, **118**, 29294-29300.
64. B. J. Tan, K. J. Klabunde and P. M. A. Sherwood, *J. Am. Chem. Soc.*, 1991, **113**, 855-861.
65. N. S. Mclntyre and M. G. Cook, *Anal. Chem.*, 1975, **47**, 2208-2213.
66. K. Chen, X. Huang, C. Wan and H. Liu, *Chem. Comm*, 2015, **51**, 7891-7894.
67. Y. Pan, Y. Liu, J. Zhao, K. Yang, J. Liang, D. Liu, W. Hu, D. Liu, Y. Liu and C. Liu, *J. Mater. Chem. A*, 2015, **3**, 1656-1665.
68. Y. Lu, J.-p. Tu, Q.-q. Xiong, H. Zhang, C.-d. Gu, X.-l. Wang and S. X. Mao, *CrystEngComm*, 2012, **14**, 8633.
69. Y. Pan, Y. Liu and C. Liu, *J. Power Sources*, 2015, **285**, 169-177.
70. C. Zhu, D. Wen, S. Leubner, M. Oschatz, Wei Liu, Matthias Holzschuh, Frank, Simon, Stefan Kaskel and a. A. Eychmüller, *Chem Commun (Camb)*, 2015, **51**, 7851-7854.
71. T. Y. Ma, S. Dai, M. Jaroniec and S. Z. Qiao, *Angew. Chem. Int. Ed.*, 2014, **53**, 7281-7285.
72. C. C. McCrory, S. Jung, J. C. Peters and T. F. Jaramillo, *J. Am. Chem. Soc.*, 2013, **135**, 16977-16987.
73. M. Gao, W. Sheng, Z. Zhuang, Q. Fang, S. Gu, J. Jiang and Y. Yan, *J. Am. Chem. Soc.* , 2014, **136**, 7077-7084.
74. I. A. Solutions, A. Damjanovic, V. I. Birss and D. S. Boudreaux, *J. Electrochem. Soc.*, 1991, **138**, 2549-2555.
75. Y. Surendranath, M. W. Kanan and D. G. Nocera, *J. Am. Chem. Soc.*, 2010, **132**, 16501-16509.
76. C. G. Morales-Guio, L. A. Stern and X. Hu, *Chem. Soc. Rev.*, 2014, **43**, 6555-6569.
77. H. Vrubel, T. Moehl, M. Gratzel and X. Hu, *Chem Commun (Camb)*, 2013, **49**, 8985-8987.
78. Y. Li, H. Wang, L. Xie, Y. Liang, G. Hong and H. Dai, *J. Am. Chem. Soc.*, 2011, **133**, 7296-7299.
79. Y. Yan, X. Ge, Z. Liu, J. Y. Wang, J. M. Lee and X. Wang, *Nanoscale*, 2013, **5**, 7768-7771.
80. J. Yang, D. Voiry, S. J. Ahn, D. Kang, A. Y. Kim, M. Chhowalla and H. S. Shin, *Angew. Chem. Int. Ed.*, 2013, **52**, 13751-13754.
81. Y. Leng, G. Chen, A. J. Mendoza, T. B. Tighe, M. A. Hickner and C. Y. Wang, *J. Am. Chem. Soc.*, 2012, **134**, 9054-9057.
82. J. Tian, Q. Liu, A. M. Asiri and X. Sun, *J. Am. Chem. Soc.* , 2014, **136**, 7587-7590.
83. Z. Huang, Z. Chen, Z. Chen, C. Lv, H. Meng and C. Zhang, *ACS NANO*, 2014, **8**, 8121-8129.

Electronic supplementary material

Ultrathin cobalt phosphide nanosheets as efficient bifunctional catalysts for water electrolysis cell and the origin for cell performance degradation

Jinfa Chang,[a,b] *Liang Liang,*[b] *Chenyang Li,*[b] *Minglei Wang,*[b] *Junjie Ge,*[b] *Changpeng Liu*[b,*] *and Wei Xing*[a,b,*]

[a] State Key Laboratory of Electroanalytical Chemistry, Changchun Institute of Applied Chemistry, Chinese Academy of Sciences, Changchun 130022 (P.R. China)

E-mail address: xingwei@ciac.ac.cn (W. Xing)

[b] Laboratory of Advanced Power Sources, Jilin Province Key Laboratory of Low Carbon Chemical Power Sources, Changchun Institute of Applied Chemistry, Chinese Academy of Sciences, Changchun 130022, PR China;

E-mail: liuchp@ciac.ac.cn (C. Liu)

Experimental Section

Materials: Sodium hypophosphite monohydrate (≥ 99.0%, $NaH_2PO_2 \cdot H_2O$), cobalt nitrate hexahydrate (≥ 98.0%, $Co(NO_3)_2 \cdot 6H_2O$), iridium oxide nanoparticles (IrO_2) and urea ($CO(NH_2)_{2)}$ were purchased from Aldrich Chemical Co. (USA). Vulcan carbon powder XC-72 (denoted as carbon) was purchased from Cabot Co. (USA). Nafion solution (5%) and PTFE (10%) was purchased from Dupont Co. (USA). Potassium hydroxide (≥ 95.0%, KOH) and ethanol (≥ 99.7%) were purchased from Beijing Chemical Co. (China). All the chemicals were of analytical grade and used as received. Highly purified N_2, O_2, and O_2/ N_2 (O_2, 1.0 mol %) were supplied by Changchun Juyang Co Ltd. Ultrapure water (resistivity : $\rho \geq 18$ MΩ cm^{-1}) was used to prepare the solutions.

Synthesis of CoP NS

The CoP NS was synthesized as described in Ref. [1] with slightly modification. Specifically, the CoP NS was prepared as follows: 2 mmol $Co(NO_3)_2 \cdot 6H_2O$ was dissolved in 160 mL water and subsequently heated to 80 ^oC under magnetic stirring. Then, 22 mL of 8 M NaOH was added to the solution. After stirring for 10 min, the precipitate was collected and dried, followed by centrifuging and washing with water for several times, then the Co_3O_4 NS was obtained. To prepare CoP NS, Co_3O_4 NS and $NaH_2PO_2 \cdot H_2O$ were placed at two separate positions in one closed porcelain crucible with $NaH_2PO_2 \cdot H_2O$ located at the upstream side of the furnace. The molar ratio for Co to P was 1:5. Subsequently, the samples were heated to 300 ^oC and rest at the temperature for 2 h under a static N_2 atmosphere. After the heat treatment, the oven was later cooled to room temperature under the protection of flowing N_2. Finally, the CoP NS was passivated in a 1.0 mol % O_2/ N_2 mixture at 20 mL min^{-1} for 3 h at room temperature.

The equation for the formation of CoP is shown as follows:

$$12Co_3O_4 + 69\ NaH_2PO_2 \rightarrow 36\ CoP + 23Na_3PO_4 + 10H_3PO_4 + 6H_2O.$$

To complete the reaction, a molar ratio at approximately 1:2 between Co and P precursors is needed. When the temperature was higher than 200 ^oC, the decomposition of NaH_2PO_2 occurs as a side reaction. Therefore, to ensure the complete conversion of Co_3O_4 NS into CoP NS, excessive NaH_2PO_2 was needed. Hence, molar ratio at 1:5 for Co:P precursors was selected. In fact, molar ratio at 1:5 was used widely in the

synthesis of CoP, as suggested in literature[1, 2]. During the reaction, the NaH_2PO_2 may decompose and release P containing molecule (PH_3). In order to restrain PH_3, excessive cupric sulfate solution ($CuSO_4$) was used at the stern of tube furnace to convert PH_3 into H_3PO_4. The reaction can be express as follows:

$$4CuSO_4 + PH_3 + 4H_2O \rightarrow 4Cu\downarrow + H_3PO_4 + 4H_2SO_4$$

As a result, the noxious gas is transformed into H_3PO_4 before entering into the atmosphere. Therefore, we claim that the CoP NS was synthesized using a simple and green approach.

Physical characterizations

AFM images were obtained with a Veeco Dimension 3100 instrument with a silicon cantilever operated in tapping mode. Scanning electron microscopy (SEM) measurements were performed with an XL 30 ESEM FEG field emission scanning electron microscope. Transmission electron microscopy (TEM), high resolution transmission electron microscopy (HR-TEM), Fast Fourier Transformation analyzer (FFT), high-annular dark-field scanning transmission electron microscopy (STEM) and element mapping analysis were conducted on Philips TECNAI G2 electron microscope operating at 200 kV. X-ray diffraction (XRD) measurements were performed with a PW-1700 diffractometer using a Cu K_α (λ=1.5405 Å) radiation source (Philips Co.). The textural and morphological features of the CoP NS were determined by nitrogen physisorption at 77 K in a Micromeritics ASAP 2020. Textural properties such as the specific surface area pore volume and pore size distribution were calculated from each corresponding nitrogen adsorption−desorption isotherm, applying the Brunauer−Emmett−Teller (BET) equation and the Barrett−Joyner−Halenda (BJH). X-ray photoelectron spectroscopy (XPS) measurements were carried out on Mg K_α radiation source (Kratos XSAM-800 spectrometer).The bulk compositions were evaluated by inductively coupled plasma optical emission spectrometer (ICP-OES, X Series 2, Thermo Scientific USA). In order to probe and compare the electrical resistance of IrO_2 and CoP, a typical four-probe method (performed on KDY-1-type four-probe resistivity/square resistance tester, Guangzhou KunDe Co., Ltd. China) was used and measurements at ambient temperature (ca. 25 ^oC). The powder samples were pressed into pellets with a diameter of 10 mm and a thickness of about 3 mm under a pressure of $4.9x10^8$ Pa. Each sample was test five times and the average value was used.

It should be noted that all the products were saved in vacuum oven at 25 ^{o}C. Due to the same result of intermediate product to Ref [1], we didn't show the XRD, TEM and SEM characterization of intermediate Co_3O_4 NS here.

Electrochemical measurements

Electrochemical measurements were performed with EG & G PARSTAT 4000 potentiostat/galvanostat (Princeton Applied Research Co., USA). A conventional one-component three-electrode cell was used, including a glassy carbon electrode (GCE, geometric area = 0.07 cm^2) as the working electrode, a platinum foil was used as the auxiliary electrode and a mercuric oxide (Hg/HgO, 1 M KOH) electrode was used as the reference electrode. To prepare the working electrode, 5 mg of the catalyst and 100 μL of 5 wt% Nafion solution were dispersed in 900 mL of ethanol solvent, followed by ultrasounded at least 30 min. Then 10 μL of the ink was dropped onto a GCE (~loading: 0.71 mg cm^{-2}). In order to enhanced the electroconductibility of CoP NS, physical mixing CoP NS with carbon (mass ratio, 1:1) was employed. The electrolyte (1 M KOH) was degassed by bubbling O_2 for at least 30 minutes before the electrochemical measurements. Prior recording the OER activity of CoP NS, the catalysts were activated by 20 CV scans along the potential window of 0.3 to 0.9 V vs. Hg/HgO in 1 M KOH at a scan rate of 100 mV s^{-1}, then the linear sweep voltammetry (LSV) with a scan rate of 5 mV s^{-1} was performed in a range from 0.3 to 0.9 V vs. Hg/HgO. During electrochemical experiments, the electrolyte was agitated using a magnetic stirrer rotating at 300 rpm. Durability test was then carried out by cyclic voltammetry (CV) scanning from 0.35 to 0.85 V vs. Hg/HgO for 1000 cycles at a scan rate of 100 mV s^{-1}. The durability of CoP NS/C was also investigated through chronopotentiometry, the time-dependent voltage was recording under a static current density of 10 mA cm^{-2} for 24 hours. The electrochemical impedance spectroscopy (EIS) measurements were carried out from 100000 to 0.1 Hz in 1 M KOH. In all measurements, Hg/HgO was used as the reference, and all the potentials reported in our work were vs. the reversible hydrogen electrode (RHE). In 1 M KOH (pH = 13.61), E(RHE) = 0.098 + 0.059*pH. Ohmic drop was corrected using the current interrupt method.

The generated gas was confirmed by gas chromatography analysis and measured quantitatively using a calibrated pressure sensor to monitor the pressure change in the anode compartment of a H-type electrolytic

cell. The glass carbon sheet (1*2 cm) was used as working electrode with a catalysts loading of 0.71 mg cm^{-2}. The Faradaic efficiency was calculated by comparing the amount of measured oxygen with calculated oxygen generated at a constent oxidative current of 10 mA cm^{-2} in 1 M KOH for 100 min electrolysis (assuming 100% FE). Pressure data during electrolysis were recorded using a CEM DT-8890 Differential Air Pressure Gauge Manometer Data Logger Meter Tester with a sampling interval of 1 point per second.

Prior to the use of titanium felt (Alfa Aesar, porosity 95%, purity 95%) as catalyst support, the titanium felt were pretreated in acetone, ethanol for 1 hour respectively and were rinsed with deionized water thoroughly. To evaluate the bifunctionality of CoP NS in alkaline solutions, the catalyst was first dispersed in ethanol, and the suspension was loaded on two 1*2 cm titanium felt sheet. The loading on both anode and cathode was at 0.71 mg cm^{-2}. To ensure the binding between the catalyst and the titanium felt sheet support, 1.5 mL of PTFE (10%) was dropped onto each electrode, after which the titanium felt sheet was heat treated at 250 ^{o}C for 1 hour. The LSV experiments were performed with a potential window range from 0.5 to 1.8V at a scan rate of 5 mV s^{-1} in 1 M KOH. The stability of the electrolyzer was examined using galavanostatic experiments in the same electrolyte. The current density was kept constant at 10 mA cm^{-2} over 24 hours of electrolysis.

Fabrication of membrane electrode assembly (MEA) with catalyst-coated substrate (CCS) method

The MEA was prepared according to the Reference[3]. CoP NS was used both as anode catalyst for oxygen evolution reaction (OER) and as cathode catalysts for hydrogen evolution reaction (HER). The untreated carbon paper (TGPH#90, Toray Inc., Japan) and titanium (Ti) foam were employed as anode and cathode gas diffusion layer (GDL), respectively. A YAB membrane (Foma Corporation, Germany) with a thickness of 0.13~0.15 mm was used as anion exchange membrane (AEM). The catalysts were mixed with deionized water, isopropanol and PTFE ionomer suspension (10 wt % polymer in suspension) to obtain well dispersed ink using magnetic stirring combined with ultrasonication. The as prepared ink was coated onto the surface of Ti foam and Toray TGP90 plain carbon paper using a spray gun to obtain a CCS for both anode and cathode. The binder content (10 wt% PTFE ionomer) was at approximately 5 wt% polymer for

both anode and cathode catalysts layer. The catalysts loading was controlled at 5 mg/cm^2 for the anode and cathode catalysts layer. The catalyst-coated substrate was heat treated at 250 ^{o}C for 1 hour. The size of all electrode catalysts layer was π× 2 cm × 2 cm (i.e. 12.56 cm^2 active areas). Anode CCS, YAB membrane and cathode CCS were assembled together in the cell hardware to form an MEA (See Fig. S 9). For comparison, a water electrolysis cell with Pt black as cathode catalyst and IrO_2 as anode catalyst was selected as the 'reference' MEA, the catalyst loading, gas-diffusion electrodes, membrane, preparation technology and the test condition of the 'reference' MEA are all same to the bifunctional CoP NS catalyst.

Cell performance evaluation

The water electrolysis cell setup is shown in Fig.. S9, which was used to evaluate the performance and durability of the single water electrolysis cell (See Fig. S 9b and 9c). Cell potential and current was controlled through an Arbin testing system (Arbin Instruments, United States). 1 M KOH was supplied into anode chamber at a flow rate of 5 mL min^{-1} with a peristaltic pump (BT100-2J, LongerPump Co. China). The cell temperature was maintained at 50 °C. Before the polarization measurements, the electrolysis cell was pretreated at 100 mA cm^{-2} for 4 h to activate the catalyst layer. The polarization curves (current density vs. cell voltage) were obtained using the Arbin testing system in galvanodynamic mode, i.e., the steady-state polarization curve was measured by recording the cell potential for 1 min from the circuit voltage under constant current density. For the durability tests, a constant current of 300 mA cm^{-2} was applied onto the electrolysis cell, and the cell voltage as a function of test time was recorded by Arbin testing system. Before the durability tests, resistance was monitored by a milliohm meter (Agilent 4338B, United States), the polarization curve was corrected with i-R drop.

In order to investigated the origin of cell degradation, the sample after electrolysis was collected by scraping off the surface layer from the carbon paper or Ti foam with a sharp knife. The XRD, SEM, TEM, XPS were performed afterward.

Table S1. Summarize the elements contents of the CoP NS.

	elements content					
element	Co[a]	P[a]	O[a]	Co[b]	P[b]	O[b,c]
Wt (ppm)	-	-	-	650100	324600	25300
Wt. %	-	-	-	65.01	32.46	2.53
At. %	47.61	38.03	14.36	47.77	45.38	6.85

a. Derived from XPS;

b. Derived from ICP-OES.

c. When we analysis the element content using ICP-OES, the testing sample undergoes high temperature fusion and dissolution process in water. Hence, a list of non-metal elements, such as H, C, N, O, F and so on, cannot be detected. Furthermore, it is shown that it is harder to excite the non-metal elements (such as H, C, N, O, etc.) into the excited state due to the high electron negativity. However, the emission spectra (transition from excited states back to the ground state) of these elements locate in the far infrared region, which is not within ICP-OES spectra range. Therefore, generally speaking, elements including H, C, N, O, etc. cannot detected by ICP-OES. If we hypothesize that only Co, P and O three elements were present in the sample, then, the content of O element can be calculated through 100% - Co% - P%. Therefore, in order to measure the O content in the sample, we repeated the tests through ICP-OES. The elements content (wt %) were calculated through the X/M*100%, where X is the content of Co and P, respectively, while M is the total weight of sample. As shown in Table S1, the elements content (at%) of Co, P and O is 47.77%, 45.38% and 6.85%, in sequence. These results are consistent with the XRD result where only partially surface passivation was observed.

Table S2. Comparison of OER activities of CoP NS/C catalysts with recently publication in alkaline conditions (The current density of 10 mA cm^{-2} was chosen because it represents the current density from a device with 12% solar to hydrogen efficiency, which is at the upper end of a realistic device[4]).

Materials	Overpotential @ 10 mA cm^{-2}	Electrolyte (M, KOH)	References
CoP NS	361	1	
CoP NS/C	277	1	This work
IrO_2	320	1	
IrO_2	320	0.1	[5]
IrO_2-CNT	360	1	[6]
g-C_3N_4 NS-	370	1	
CoOx@CN	410	1	[7]
NiOx	360	0.5	[8]
Ni-Co_2-O	362	1	[9]
Co_3O_4/graphene	310	1	[10]
N-CG-CoO	340	1	[11]
Co_3O_4C-NA	290	1	[12]
CoMn-LDH	324	1	[13]
NiCo-LDH	367	1	[14]
$NiCo_2O_4$	565	1	[15]
NiFe-LDH	320	1	[16]
Co_3O_4/2.7Co_2MnO_4	540	0.1	[17]
α-Fe_2O_3 NA/CC	420	1	[18]
$Mn_{0.1}Ni_1$	420	0.1	[19]
3D NF/PC/AN	407	1	[20]
CoP NP	340		
CoP NR	320	1	[21]

Table S3 Comparison of HER activities of CoP NS/C catalysts with recently publication in alkaline conditions.

Materials	Overpotential (V)	@ XX mA cm^{-2}	Tafel slope (mV dec^{-1})	Electrolyte (M, KOH or NaOH)	References
CoP NS/C	0.111	10	70.9	1	This work
	0.139	20			
PCPTF	0.430	30	N.A.	1	[22]
NiS_2 NA/CC	0.149	10	104	1	[23]
Ni_3S_2/Ni foam	0.123	10	110	1	[24]
NiSe/NF	0.096	10	120	1	[25]
Ni_2P	0.220	10	N.A.	1	[26]
WN NA/CC	0.285	10	170	1	[27]
Ni_5P_4	0.150	10	N.A.	1	[28]
Mn_1Ni_1	0.420	20	N.A.	0.1	[19]
Ni_5P_4	0.049	10	98	1	[29]
Ni_2P	0.069		118		
CoO_x@CN	0.232	10	N.A.	1	[7]
N-Co@G	0.337	10	N.A.	0.1	[30]
Co-NRCNTs	0.450	20	N.A.	1	[31]
CoP/CC	0.209	10	129	1	[32]
C_3N_4/TiO_2	0.300	1.3	N.A.	0.1	[33]
WP NAs/CC	0.150	10	102	1	[34]
FeP NAs/CC	0.218	10	146	1	[35]
NiO/Ni-CNT	0.125	20	82	1	[36]
Ni_2P–G@NF	0.150	20	30	1	[37]
np-CoP/Ti	0.150	20	71	1	[38]

Table S4 Compare the binding energy and elemental content for Co 2p, P 2p and O 1s of the fresh prepared CoP NS with the CoP NS that after electrolysis on cathode HER side and anode OER side. (The elemental content was obtained by deconvolution the Co, P and O singal)

	Co 2P $_{3/2}$	Co_3O_4 2p $_{3/2}$	Co_3O_4 satellite	Phosphide		orthophosphate		Lattic O	Adsorbed O
Fresh prepared CoP	36.73% 777.4 eV	63.27% 780.9 eV	--	66.67%		33.33%		71.39% 531.4 eV	28.61% 532.9 eV
				129.8 eV	130.9 eV	133.3 eV	134.4 eV		
After HER electrolysis side of CoP	73.49% 777.3 eV	26.51% 780.8 eV	--	61.09%		38.91%		62.45% 531.1eV	37.55% 532.6 eV
				129.7 eV	130.8 eV	133.2 eV	134.3 eV		
After OER electrolysis side of CoP	25.10% 778.6 eV	58.03% 782.1 eV	16.87% 786.4 eV	22.28%		77.72%		65.99% 531.0 eV	34.01% 532.5 eV
				129.1 eV	130.2 eV	133.0 eV	134.3 1 eV		

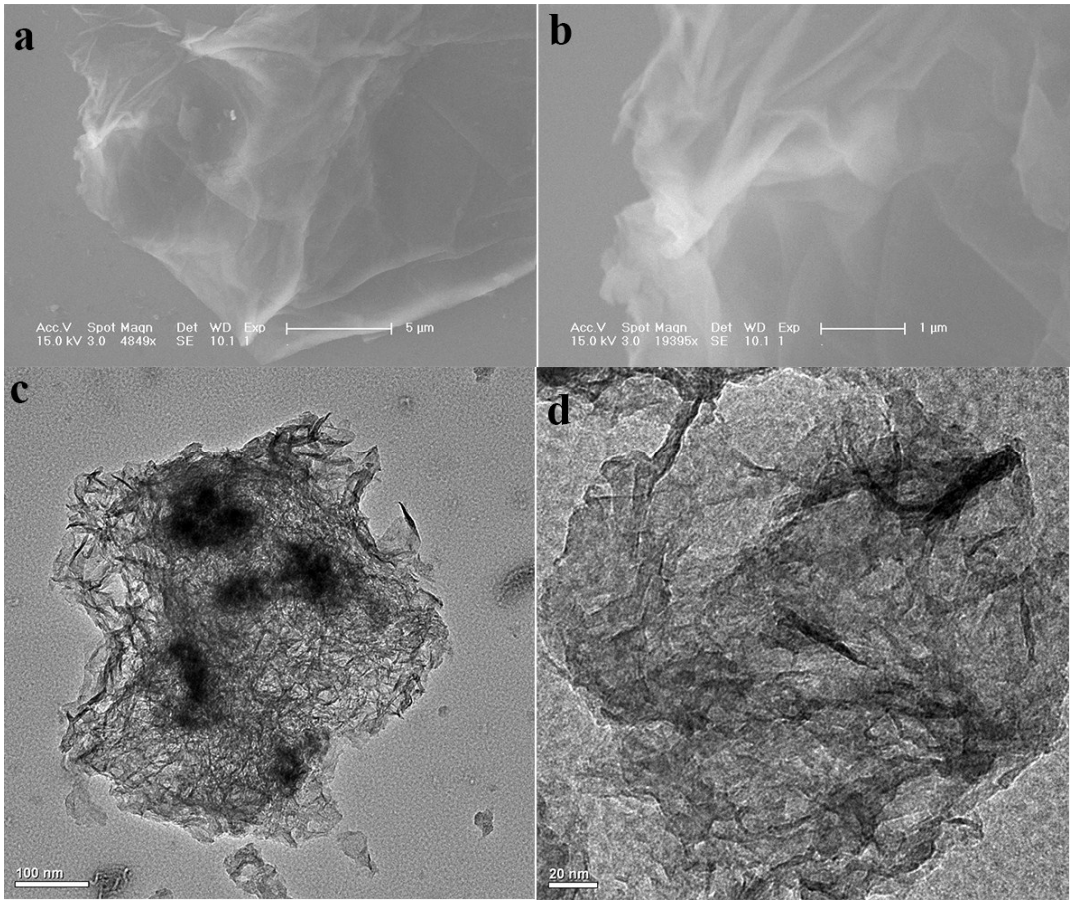

Fig. S1 SEM (a and b) and TEM (c and d) images for frehsh prepared CoP NS.

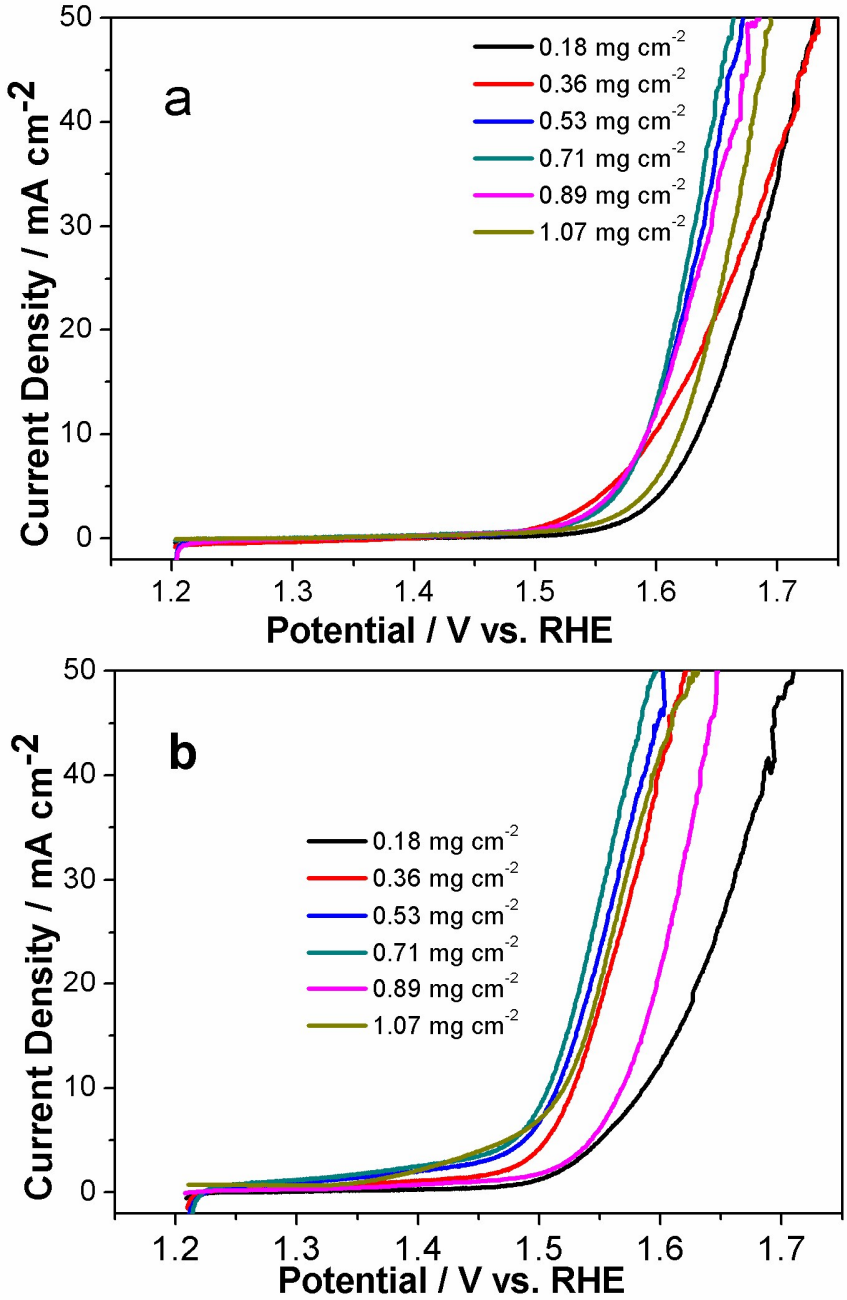

Fig. S2. Polarization curves of CoP NS (a) and CoP NS/C (b) in oxygen saturated 1 M KOH solution with different catalysts loading on GC; scanning rate was 5 mV s^{-1} and Potentials were corrected with iR drop.

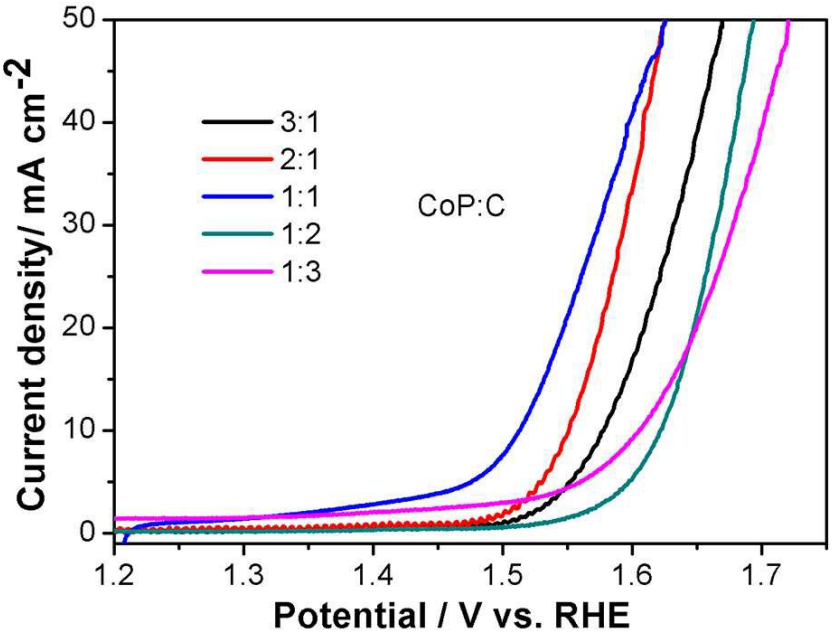

Fig. S3 OER performance for CoP NS/C with different CoP NS and C mass ration in 1 M O_2-saturated KOH. The scan rate was 5 mV s^{-1} and catalysts loading was 0.71 mg cm^{-2}.

As can be seen from the above figure, mass ratio effect of CoP : C on water splitting exhibits a volcano-shaped curve, with the optimized ratio located at 1:1. While mass ratios at >1 provide insufficient electron conductivity, the values at <1 supply insufficient catalytic sites for the reaction, thus, leading to inferior performances on both ends. Base the above results, we have chosen the ratio at 1:1 for all following measurements.

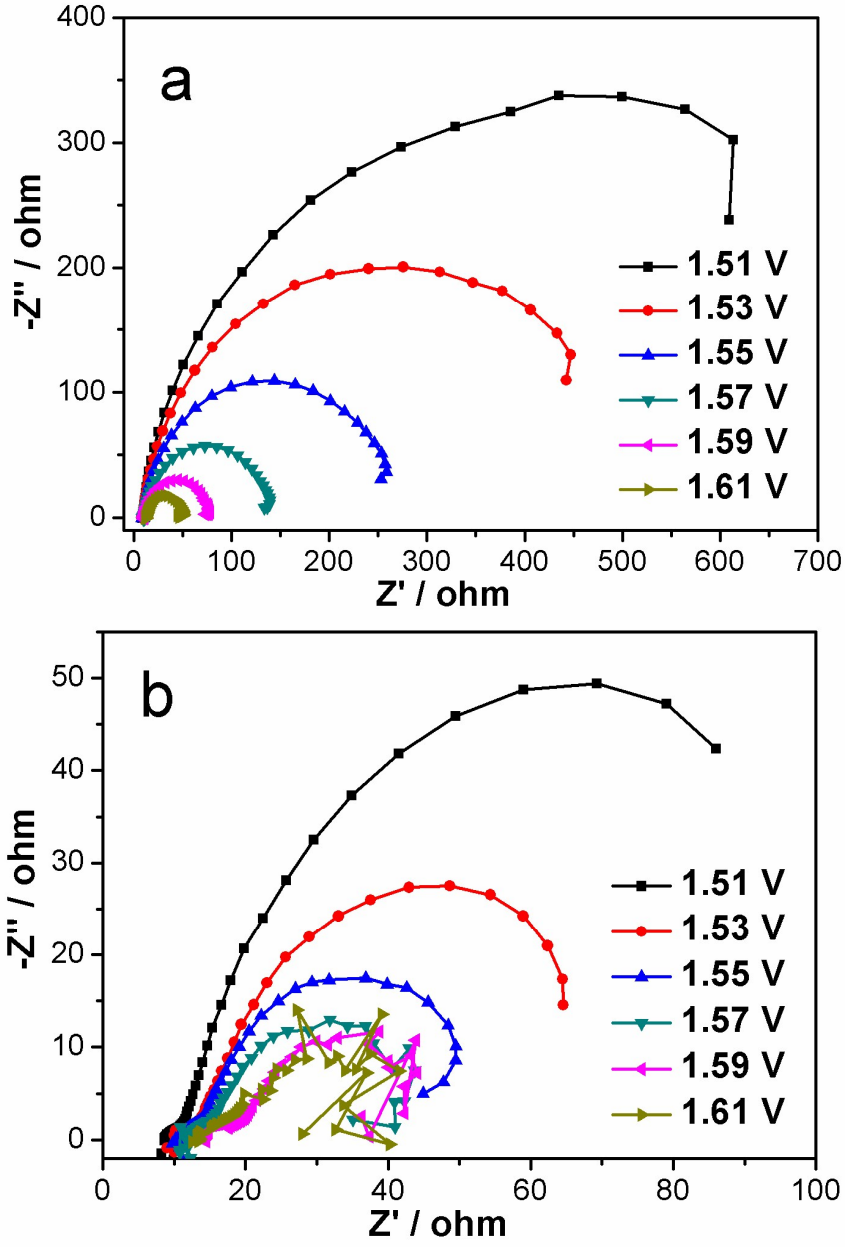

Fig. S4 Nyquist plots of the CoP NS (a) and CoP NS/C (b) in oxygen saturated 1 KOH solutions.

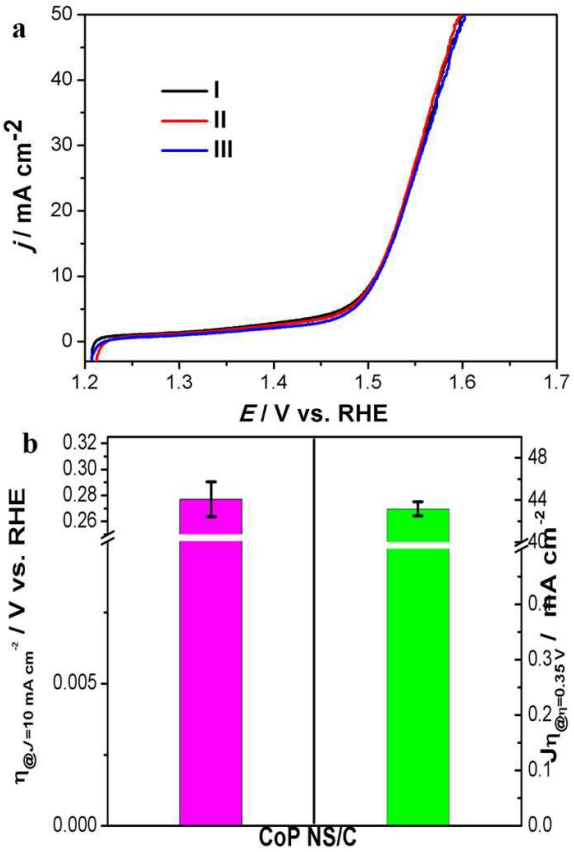

Fig. S5 a) OER performance for CoP NS/C (mass ration, 1:1) in 1 M O_2-saturated KOH solution. The scan rate was 5 mV s^{-1} and catalysts loading was 0.71 mg cm^{-2}. I, II and III represent three independent measurements respectively; b) The Over-potential required for J =10 mA cm^{-2} and current density at η = 0.35 V. The error bar represents the range of results from three independent measurements.

the electrochemical tests for each catalyst were repeated for at least three times, where high reproducibility was acquired. For instance, Fig. S5a presents three independent measurements of CoP NS/C (mass ration, 1:1), where the three polarization curves overlap almost perfectly. From Fig. S5 b, it is observed that the error was in allowance range area. Hence, we confirm that our results are credible and can be reproduced.

Fig. S6 Optical photograph showing the genration of oxygen bubbles on CoP NS/C supported on glass carbon sheets during FE test.

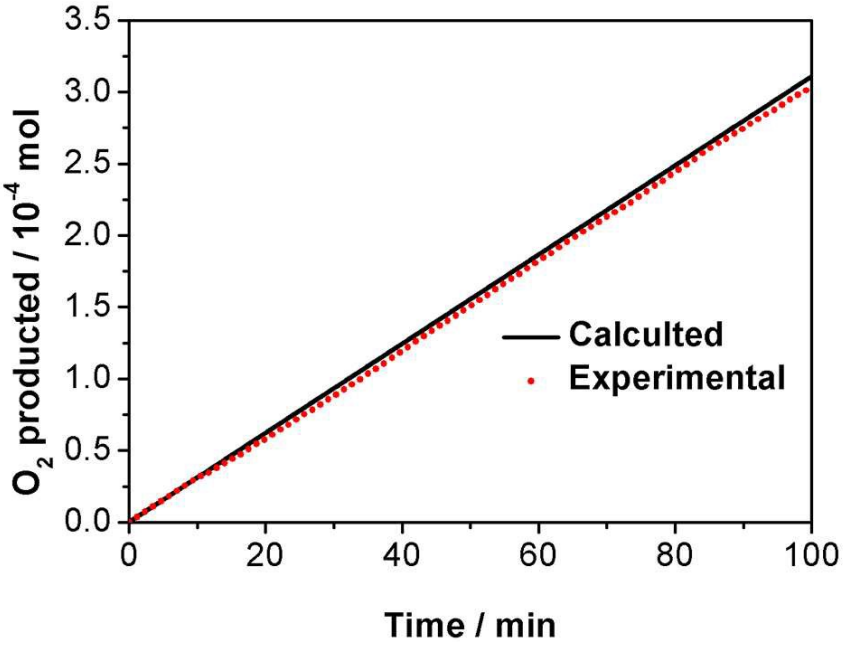

Fig. S7 Calculated versus actual oxygen production catalyzed by CoP NS/C at a constant oxidative current of 10 mA cm^{-2} in 1 M KOH for 100 min.

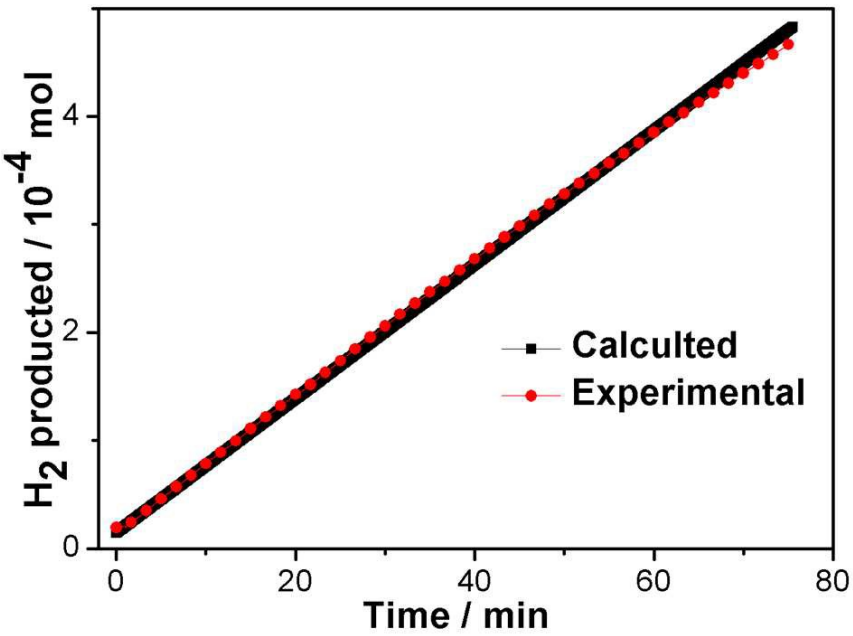

Fig. S8 Calculated versus actual hydrogen production catalyzed by CoP NS/C at a constant oxidative current of 10 mA cm^{-2} in 1 M KOH for 80 min.

Fig. S9 Potograph of a) AEMWE cell configuration, b) cathode side and c) anode side of the electrolytic cell.

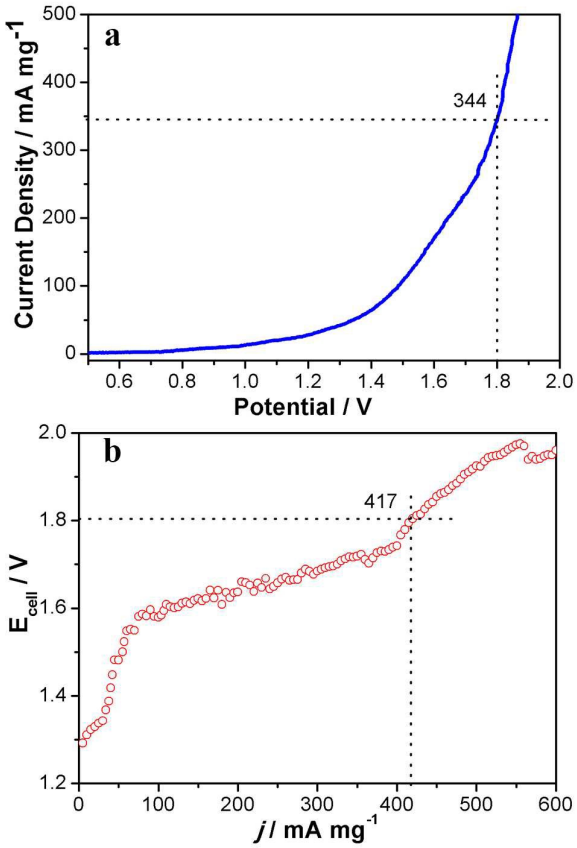

Fig. S10 Current-potential (a) response of the electrolyzer using CoP NS as catalyst both for OER and HER in 1 M KOH solutions and (b) polarization curve for a real water electrolysis cell normalize to mass activity derive from **Fig. 5a** and **Fig. 5c**.

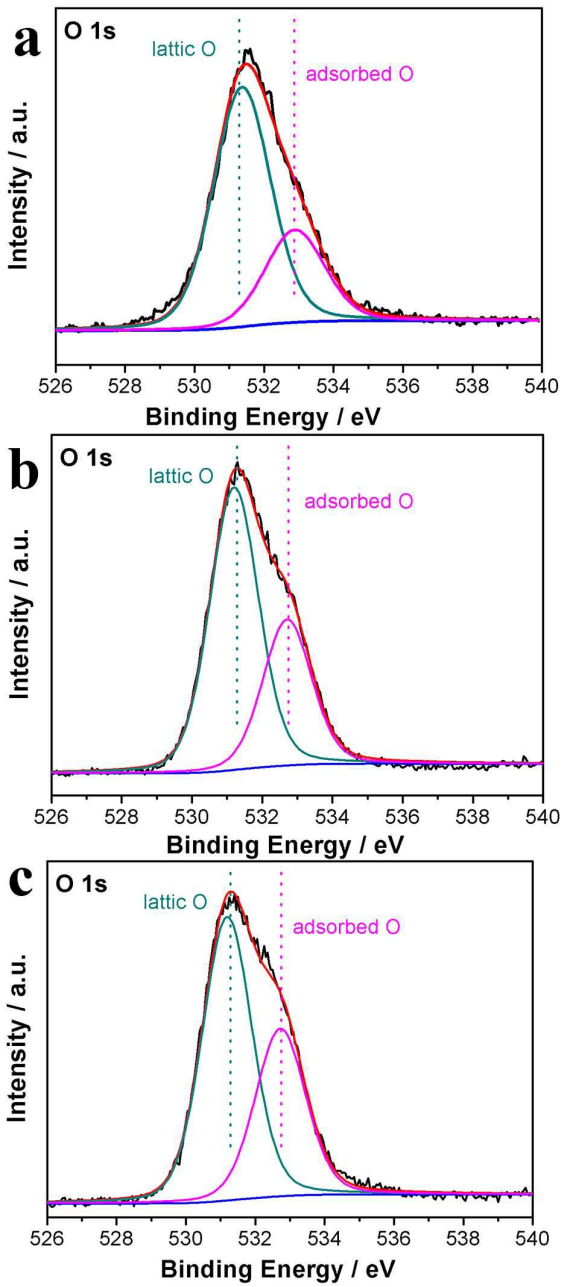

Fig. S11 Comparison the high-resolution XPS patterns for O 1s of the fresh prepared CoP NS (a) with the CoP NS that after electrolysis on cathode HER side (b) and anode OER side (c).

References

1. P. Jiang, Q. Liu, C. Ge, W. Cui, Z. Pu, A. M. Asiri and X. Sun, *J. Mater. Chem. A*, 2014, **2**, 14634-14640.
2. Q. Liu, J. Tian, W. Cui, P. Jiang, N. Cheng, A. M. Asiri and X. Sun, *Angew. Chem. Int. Ed.*, 2014, **53**, 6710-6714.
3. Y. Leng, G. Chen, A. J. Mendoza, T. B. Tighe, M. A. Hickner and C. Y. Wang, *J. Am. Chem. Soc.*, 2012, **134**, 9054-9057.
4. F. Song and X. Hu, *Nat. Commun.*, 2014, **5**, 4477.
5. Y. Gorlin and T. F. Jaramillo, *J. Am. Chem. Soc.*, 2010, **132**, 13612–13614.
6. T. Y. Ma, S. Dai, M. Jaroniec and S. Z. Qiao, *Angew. Chem. Int. Ed.*, 2014, **53**, 7281-7285.
7. H. Jin, J. Wang, D. Su, Z. Wei, Z. Pang and Y. Wang, *J. Am. Chem. Soc.*, 2015, **137**, 2688-2694.
8. K. Fominykh, J. M. Feckl, J. Sicklinger, M. Döblinger, S. Böcklein, J. Ziegler, L. Peter, J. Rathousky, E.-W. Scheidt, T. Bein and D. Fattakhova-Rohlfing, *Adv. Funct. Mater.*, 2014, **24**, 3123-3129.
9. C. Zhu, D. Wen, S. Leubner, M. Oschatz, Wei Liu, Matthias Holzschuh, Frank, Simon, Stefan Kaskel and a. A. Eychmüller, *Chem Commun (Camb)*, 2015, **51**, 7851-7854.
10. Y. Liang, Y. Li, H. Wang, J. Zhou, J. Wang, T. Regier and H. Dai, *Nat. Mater.*, 2011, **10**, 780–786.
11. S. Mao, Z. Wen, T. Huang, Y. Hou and J. Chen, *Energy Environ. Sci.*, 2014, **7**, 609-616.
12. T. Y. Ma, S. Dai, M. Jaroniec and S. Z. Qiao, *J. Am. Chem. Soc.*, 2014, **136**, 13925-13931.
13. F. Song and X. Hu, *J. Am. Chem. Soc.*, 2014, **136**, 16481-16484.
14. H. Liang, F. Meng, M. Caban-Acevedo, L. Li, A. Forticaux, L. Xiu, Z. Wang and S. Jin, *Nano letters*, 2015, **15**, 1421-1427.
15. H. Shi and G. Zhao, *J. Phys. Chem. C*, 2014, **118**, 25939-25946.
16. M. Gong, Y. Li, H. Wang, Y. Liang, J. Z. Wu, J. Zhou, J. Wang, T. Regier, F. Wei and H. Dai, *J. Am. Chem. Soc.*, 2013, **135**, 8452-8455.
17. D. Wang, X. Chen, D. G. Evans and W. Yang, *Nanoscale*, 2013, **5**, 5312-5315.
18. Q. Liu, A. M. Asiri and X. Sun, *Electrochem. commun.*, 2014, **49**, 21-24.
19. M. Ledendecker, G. Clavel, M. Antonietti and M. Shalom, *Adv. Funct. Mater.*, 2015, **25**, 393-399.
20. J. Wang, H. X. Zhong, Y. L. Qin and X. B. Zhang, *Angew. Chem. Int. Ed.*, 2013, **52**, 5248-5253.
21. J. Chang, Y. Xiao, M. Xiao, J. Ge, C. Liu and W. Xing, *ACS Catalysis*, 2015, **5**, 6874-6878.
22. Y. Yang, H. Fei, G. Ruan and J. M. Tour, *Adv. Mater.*, 2015, **27**, 3175-3180.
23. C. Tang, Z. Pu, Q. Liu, A. M. Asiri and X. Sun, *Electrochimica Acta*, 2015, **153**, 508-514.
24. C. Tang, Z. Pu, Q. Liu, A. M. Asiri, Y. Luo and X. Sun, *Int. J. Hydrogen Energy* 2015, **40**, 4727-4732.
25. C. Tang, N. Cheng, Z. Pu, W. Xing and X. Sun, *Angew. Chem. Int. Ed.*, 2015, **127**, 9483-9487.
26. L.-A. Stern, L. Feng, F. Song and X. Hu, *Energy Environ. Sci.*, 2015, **8**, 2347-2351.
27. J. Shi, Z. Pu, Q. Liu, A. M. Asiri, J. Hu and X. Sun, *Electrochimica Acta*, 2015, **154**, 345-351.
28. M. Ledendecker, S. Krick Calderon, C. Papp, H. P. Steinruck, M. Antonietti and M. Shalom, *Angew. Chem. Int. Ed.*, 2015, **127**, 12538-12542.
29. A. B. Laursen, K. R. Patraju, M. J. Whitaker, M. Retuerto, T. Sarkar, N. Yao, K. V. Ramanujachary, M. Greenblatt and G. C. Dismukes, *Energy Environ. Sci.*, 2015, **8**, 1027-1034.
30. H. Fei, Y. Yang, Z. Peng, G. Ruan, Q. Zhong, L. Li, E. L. Samuel and J. M. Tour, *ACS applied materials & interfaces*, 2015, **7**, 8083-8087.
31. X. Zou, X. Huang, A. Goswami, R. Silva, B. R. Sathe, E. Mikmekova and T. Asefa, *Angew. Chem. Int. Ed.*, 2014, **53**, 4372-4376.
32. J. Tian, Q. Liu, A. M. Asiri and X. Sun, *J. Am. Chem. Soc.* , 2014, **136**, 7587-7590.
33. M. Shalom, S. Gimenez, F. Schipper, I. Herraiz-Cardona, J. Bisquert and M. Antonietti, *Angew. Chem. Int. Ed.*, 2014, **53**, 3654-3658.
34. Z. Pu, Q. Liu, A. M. Asiri and X. Sun, *ACS Appl. Mater. Interfaces*, 2014, **6**, 21874-21879.
35. Y. Liang, Q. Liu, A. M. Asiri, X. Sun and Y. Luo, *ACS Catalysis*, 2014, **4**, 4065-4069.
36. M. Gong, W. Zhou, M. C. Tsai, J. Zhou, M. Guan, M. C. Lin, B. Zhang, Y. Hu, D. Y. Wang, J. Yang, S. J. Pennycook, B. J. Hwang and H. Dai, *Nat. Commun.*, 2014, **5**, 4695.
37. A. Han, S. Jin, H. Chen, H. Ji, Z. Sun and P. Du, *J. Mater. Chem. A*, 2014, **3**, 1941-1946.
38. S. Gu, H. Du, A. M. Asiri, X. Sun and C. M. Li, *Phys. Chem. Chem. Phys.*, 2014, **16**, 16909-16913.

Ultrathin CoP nanosheet is prepared by a green and facile approach and found to be an effective and robust bifunctional catalyst material for OER and HER in basic solution.